Planetary and Space Science 281 (2026) 106318

Contents lists available at ScienceDirect

Planetary and Space Science

journal homepage: www.elsevier.com/locate/pss

A novel production strategy for high-porosity simulants of Ryugu surface boulders☆

Moritz Goldmann [a,*], Markus Patzek [a], Ansgar Greshake [b], Bhuvan Agrawal [c], Jens Biele [d], Jürgen Blum [e], Dominik Dieter [b], Matthias Grott [c], Carsten Güttler [a], Jörg Knollenberg [c], Bastian Gundlach [a]

[a] University of Münster, Institut für Planetologie, Wilhelm-Klemm-Straße 10, Münster, 48149, Germany
[b] Museum für Naturkunde, Leibniz-Institut für Evolutions- und Biodiversitätsforschung, Invalidenstraße 43, Berlin, 10115, Germany
[c] German Aerospace Center, Institute of Space Research, Rutherfordstraße 2, Berlin, 12489, Germany
[d] German Aerospace Center, Space Operations and Astronaut Training, Köln, 51147, Germany
[e] TU Braunschweig, Institut für Geophysik und Extraterrestrische Physik, Mendelssohnstraße 3, Braunschweig, 38106, Germany

ARTICLE INFO

Keywords:
Asteroid simulant
Modal mineralogy
Grain size distribution
Grain shape distribution
Microstructural characterisation

ABSTRACT

This study presents a strategy to produce artificial rocks, or simulants, designed to replicate boulders observed on the surface of asteroid Ryugu. The simulants are composed of a dust mixture with bulk composition and grain size distribution based on the analysis of particles returned from Ryugu by the Hayabusa2 mission. Two production methods, freeze-drying and dry-compression, were established to generate simulants with porosities between 45% and 80%. Five key parameters were used to characterise the simulants and to compare them with Ryugu particles: the bulk composition of the dust mixture, the size and shape distribution of the individual components, the simulant microstructure, i.e. the internal distribution of material and void spaces, and the interaction between the grains within the simulant. These parameters were assessed using scanning electron microscopy, laser diffraction, helium gas pycnometry, and micro-tomographic analysis. Even though some discrepancies in composition and grain size distribution remain, these can be addressed in future updates of the simulant dust mixture. It was generally found that freeze-dried simulants capture the microstructure and grain interactions of Ryugu particles better than the dry-compressed simulants. In a next step, thermal and mechanical properties of the simulants will be measured to support the interpretation of remote sensing observations of Ryugu's surface.

1. Introduction

The study of asteroids has long been an integral part of planetary science, providing valuable insights into the formation and evolution of our solar system. Advances in space exploration have enabled unprecedented close-up observations of these ancient bodies, revolutionising our understanding of their composition and structure. The successful return of samples from Itokawa (visited by the Hayabusa spacecraft between 2005–2007; Yoshikawa et al., 2021), Ryugu (visited by the Hayabusa2 spacecraft between 2018–2019; Tachibana, 2021), and Bennu (visited by the OSIRIS-REx spacecraft between 2018–2021; Lauretta et al., 2021) represents a major breakthrough in this field of research, offering scientists a unique opportunity to analyse extraterrestrial materials firsthand. Besides returned samples from asteroids by space missions, meteorites offered and still offer an important way to study extraterrestrial materials. Unlike freshly fallen and recovered meteorites (e.g. Tagish Lake, Hildebrand et al., 2006; Tarda, Marrocchi et al., 2021) most meteorites suffered from terrestrial alteration (King et al., 2020) that modified their primary mineralogy and composition as well as their physical properties. Considering the limited mass returned from space missions to asteroids, meteorites are nonetheless important to derive physical and mineralogical features of different asteroid types. However, they likely lack specific features present on asteroid surfaces due to atmospheric filtering of meteoroids during atmospheric entry, during which up to around 80 % of the meteoroid can be ablated (Rogers et al., 2005). Yet despite the advancements from recent sample return missions, many questions remain unanswered, especially concerning the internal structure and mechanical properties of certain groups of asteroids.

☆ This article is part of a Special issue entitled: 'Planetary Simulants' published in Planetary and Space Science.

* Corresponding author.
E-mail address: moritz.goldmann@uni-muenster.de (M. Goldmann).

https://doi.org/10.1016/j.pss.2026.106318
Received 26 March 2026; Received in revised form 15 June 2026; Accepted 28 July 2026
Available online 8 August 2026
0032-0633/© 2026 The Authors. Published by Elsevier Ltd. This is an open access article under the CC BY license (http://creativecommons.org/licenses/by/4.0/).

The chemically most pristine and largest group, comprising approximately 75 % of all known asteroids, are the C-type asteroids. Until the arrival of Hayabusa2 at Ryugu and OSIRIS-REx at Bennu, telescopic thermal infrared observations led to the prediction of their surface covered with centimetre-sized particles (Gundlach and Blum, 2013). But instead, those bodies seem to be covered with metre-sized boulders and almost no finer grains, which together with thermal infrared data suggests a rather high boulder porosity, partially exceeding 70 % (Biele et al., 2019; Michikami et al., 2019; Grott et al., 2019; Okada et al., 2020; Rozitis et al., 2020; Sakatani et al., 2021; Cambioni et al., 2021).

This unforeseen finding compels us to reassess our understanding of the structure and strength of asteroid surfaces and specifically boulders on them. Therefore, laboratory investigations of those boulders or analogue rocks with a wide range of bulk porosities become necessary to establish a deeper understanding of how thermal properties can be used to estimate their internal structure and how mechanical properties relate to thermal properties, ultimately informing our understanding of asteroid surfaces.

Unfortunately, only six CI chondrites (Ivuna-type carbonaceous chondrites) with a total mass of about 21 kg, which are most likely related to Ryugu- and Bennu-type asteroids, have been found on Earth (Lodders et al., 2009; Pilorget et al., 2025; Gattacceca et al., 2025). Moreover, their thermal inertias exceed the values measured on the surfaces of Ryugu and Bennu by roughly a factor of three (Rozitis et al., 2020). Additionally, they contain phases not present in samples returned by Hayabusa2 and OSIRIS-REx, indicating rapid terrestrial alteration and change in, at least, their mineralogy (Pilorget et al., 2025). The retrieved samples from Ryugu (5.4 g; Yokoyama et al., 2023) and Bennu (121.6 g; Lauretta et al., 2024) are too valuable and insufficiently diverse in structure to allow systematic investigation of their porosity-dependent thermal and mechanical properties. Hence, the development of a suitable simulant material becomes imperative.

Previous studies have already addressed the production of CI simulants, as well as simulants specifically designed for Ryugu, Bennu, or the potentially closely related Martian moon Phobos to investigate properties such as bulk chemistry, spectroscopic behaviour, and mechanical strength (Hildebrand et al., 2015; Britt et al., 2019; Miyamoto et al., 2021; Miyamoto and Niihara, 2021; Wargnier et al., 2024). While each of these simulants fulfils their purpose, their underlying dust mixtures or production strategies are not suitable for achieving the simulant properties targeted in this work. Therefore, a new basic dust mixture and production method were developed. A comparison between the previous approaches and the methodology presented in this study is provided in Section 6.4.

Section 2 defines the criteria and objectives used for the simulant characterisation. Section 3 describes the selection of the basic dust components used for simulant production based on the composition of returned Ryugu particles and compares the grain sizes and shapes of Ryugu and simulant components. Section 4 presents the methods developed to produce simulants with a broad range of bulk porosities, while the structural characterisation of the resulting samples is described in Section 5. Section 6 discusses the implications and limitations of the current approach and highlights scientific possibilities and potential applications. Finally, Section 7 summarises the main findings.

2. Simulant characterisation criteria

The primary purpose of the simulant material, described in this paper, is the production of artificial rocks, which are closely related to boulders on the surface of Ryugu-type asteroids and mimic their thermal and mechanical properties and not necessarily other parameters such as spectral or magnetic properties.

The thermal and mechanical properties of the simulants are controlled by several key characteristics. In this study, the focus is set on five major aspects:

1. **The bulk composition:** The mineralogical and organic constituents determine the intrinsic thermal conductivity of the bulk material.
   To reproduce these intrinsic properties and account for potential interactions between individual components, the aim of this analogue material is to replicate all constituents of the Ryugu material that contribute at least 1 vol.%.
2. **The grain size distribution:** Smaller grains provide a larger total contact area within a given volume, enhancing both heat transfer and interparticle contact forces (Johnson et al., 1971; Sakatani et al., 2017; Haack et al., 2020). A broader size distribution can further increase the total contact area, as finer grains may fill the voids between coarser particles (Roquier, 2024).
   In order to replicate the arrangement and packing structure of the grains in the Ryugu material as accurately as possible, this study aims to reproduce the grain size distribution as precisely as possible within the limits of the available processing and measurement techniques.
3. **The grain shape distribution:** Grain morphology influences the coordination number, that is, the number of contacts per grain, and thus the total contact area, with direct consequences for heat transfer and mechanical strength (Johnson et al., 1971; Sakatani et al., 2017; Haack et al., 2020). Because the relative spatial arrangement of grains cannot be predicted a priori, its effect can only be estimated from microscopic observations.
   Analogous to the grain size distribution, reproducing the grain shape distribution is also desirable. However, unlike the grain size distribution, it cannot be directly controlled with the available methods. Therefore, the aim of this work is to achieve a comparative characterisation of grain shapes in the Ryugu material and in the developed simulant within the limits of the available measurement techniques.
4. **The microstructure of the simulant:** The microstructure describes the internal material arrangement within the simulant. It includes the density distribution within the sample as well as the porous structure, which quantifies the global ratio of void space to total volume (bulk porosity) and the spatial and size distribution of individual pores. While density inhomogeneities and gradients affect the thermal and mechanical interaction of the constituent components, the porous structure controls the overall number of grain contacts and thus influences both heat transfer and mechanical strength (Klar et al., 2024; Johnson et al., 1971; Sakatani et al., 2017; Haack et al., 2020). Although bulk porosity is influenced by the grain size and shape distributions, it can also be varied independently (Section 4).
   As the aim of this study is to reproduce the thermal and mechanical properties of boulders on the surface of Ryugu as accurately as possible, the previously described microstructural characteristics should also be approximated as closely as possible. However, as discussed in Section 5.1, returned Ryugu particles contain both regions that appear to be homogeneously mixed on the grain-size scale and regions exhibiting heterogeneous structures on length scales of 100 µm or larger. Therefore, the primary objective of this work is to first establish homogeneous structures at approximately the grain-size scale as a baseline. This also implies that, in order to achieve the desired porosity, the resulting pores should not significantly exceed the maximum grain-size and should be distributed as homogeneously as possible throughout the sample.
5. **The grain–grain contacts:** The strength of interparticle contacts, ranging from weak van der Waals forces to strong chemical or sintering bonds, directly affects both thermal conductivity and mechanical strength (Sakatani et al., 2017; German, 1996).
   The grains in the particles returned from Ryugu are not merely in contact with one another but are closely intergrown (Tomioka et al., 2023). Such grain–grain contacts can currently only be

Table 1
Simulant composition and component densities measured with an uncertainty of 5 % (elemental composition of the minerals and contaminations listed in Table A.1 in Appendix A).

Ryugu component	Simulant component	Volume fraction [vol.%]	Grain density [g cm^{-3}]	Mass fraction [wt.%]
Serpentine	Chrysotile	39	2.6	40
Saponite	Beidellite	39	2.4	36
Fe-Sulphides	Pyrite	4	4.1	6
Magnetite	Magnetite	5	4.1	9
Carbonates	Dolomite	4	2.8	4
Organics	Hard brown coal	9	1.4	5
	Total:	100	2.6	100

produced in the laboratory with considerable effort, particularly for samples of the size discussed in this work, as will be explained in more detail in Section 5.3. The aim of this study is therefore to create grain–grain contacts that are as stable as possible without violating the aforementioned constraints.

3. Simulant material selection

3.1. Composition

To reproduce the bulk composition of the material returned from Ryugu, as outlined in the previous section, the relevant constituent components must first be identified.

3.1.1. Ryugu material composition

Mineralogical analyses of 22 grains ranging from millimetres to centimetres, as well as finer dust returned from Ryugu reveal a composition dominated by fine-grained phyllosilicates (serpentine and saponite in almost equal amounts, 86 vol.%) with Mg/(Mg + Fe) ratios of around 0.85 for coarser grains, along with minor magnetite (6 vol.%), Fe-sulphides (predominantly pyrrhotite, 4 vol.%) and carbonates (mostly dolomite, 4 vol.%) (Tachibana, 2023). No significant differences between the two sampling sites were observed (Tachibana, 2023). Components contributing less than 1 vol.% are neglected in this summary.

In addition to the mineralogical composition, the organic matter content was examined. Thermogravimetric analysis coupled with mass spectrometry (TG-MS) was used to determine the proportion of carbon present in organic matter and that bound in carbonates. An organic carbon content of approximately 3 wt.% was found (Yokoyama et al., 2023). A detailed analysis of Ryugu's organic composition identified over 20,000 organic molecules whose properties are very similar to those found in CI chondrites such as Orgueil (Tachibana, 2023).

For completeness, it should be noted that the mineralogical and organic compositions observed in Bennu samples and in CI chondrites, thought to originate from Ryugu-type asteroids (Lodders et al., 2009), are very similar to those found in Ryugu samples (Lauretta et al., 2024; King et al., 2015).

3.1.2. Simulant material composition

To recreate the basic composition of Ryugu, the components shown in Table 1 are used. Because minerals with the exact composition are difficult to obtain on earth, they are partially substituted by compositionally similar analogue materials. The serpentine group is represented by a magnesium-rich serpentine with an Mg/(Mg + Fe) ratio larger 0.9, most closely resembling chrysotile. Saponite is represented by a mineral from its parent group, the smectites, most comparable to beidellite, containing only small amounts of iron and magnesium. Magnetite can be used in the same elemental composition as that found on Ryugu. The carbonates are represented by their most common member, dolomite. The Fe-sulphides are represented by pyrite, which, unlike pyrrhotite with a stoichiometric ratio close to 1:1, has a stoichiometric ratio of 1:2. The reason for this substitution lies in its manageability and availability. Metal sulphides with a stoichiometric ratio close to 1:1 oxidise much faster in air than metal sulphides with a higher sulphur content and thus change their mineralogy and properties more quickly (Belzile et al., 2004). Even though the Fe/S ratio cannot be accurately represented in this way, there is a stable Fe-sulphide in the mixture, allowing samples with the same structure to be produced from the same mixture over longer periods of time. A discussion of the influence on the bulk thermal conductivity is provided in Section 6.1. In addition to the issue of its stability, it should be noted that no supplier could be found to provide pyrrhotite powder in the required quantities at a reasonable price. Despite the shortcomings outlined above, pyrite represents a suitable alternative, as its density (~4.8 g cm^{-3}; Diment and Pratt, 1988) is comparable to that of pyrrhotite (~4.7 g cm^{-3}; Diment and Pratt, 1988), and its grain shape distribution closely matches the distribution of pyrrhotite grains observed in Ryugu particles (Section 3.2.2).

Since accurately reproducing the organic compounds described above would be highly complex and lies beyond the main focus of this study, German hard brown coal, comparable to U.S. sub-bituminous coal (Taylor et al., 1998), was selected as a simplified analogue material. Sub-bituminous coal exhibits a similar degree of aromaticity and elemental composition to the organic matter found in the CI chondrite Orgueil (Metzger et al., 2019), which, as noted earlier, shows comparable characteristics to the organic material identified in Ryugu samples.

The simulant component powders were sourced from specialised suppliers to ensure consistent quality (Table A.2 in Appendix A).

The composition of the individual minerals in the simulant material was determined and verified via backscattered electron (BSE) imaging using a *JSM-6610LV* secondary electron microscope from *JEOL Ltd.* with an acceleration voltage of 20 kV and a beam current of 1.5 nA at the Institut für Planetologie, University of Münster. The grain densities of the individual components, as well as that of the bulk dust mixture (Table 1) were measured via helium gas pycnometry using a *Micropycnometer* from *Quantachrome Instruments* at the Institute of Geotechnology and Mineral Resources, Clausthal University of Technology.

Based on the mineral volume fractions and the organic carbon content found in samples of asteroid Ryugu (Section 3.1.1) and the component densities given in Table 1, the mass fractions of the individual simulant components were calculated (Table 1). Using these mass fractions together with the corresponding component densities, the bulk density of the dust mixture was derived and was found to be consistent with the independently measured value reported in Table 1.

3.2. Grain size and shape distributions

To evaluate the similarity between the simulated dust mixture and the material returned from Ryugu, the grain size and shape distributions of both materials are characterised and compared.

3.2.1. Ryugu material grain size and shape distributions

X-ray maps of polished sections obtained from three particles returned from Ryugu (Ito et al., 2022; Yokoyama et al., 2023) are used here to estimate the size and shape distributions of magnetite, pyrrhotite, and dolomite grains. One such section is shown in Fig. 1a.

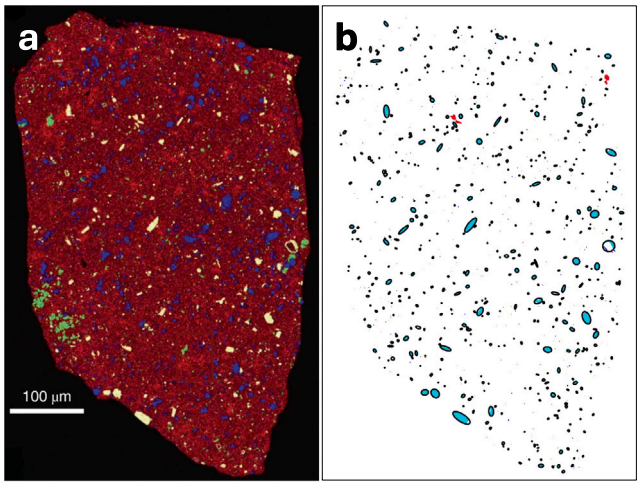

Fig. 1. (a) X-ray map composed of Mg-phyllosilicates (red), carbonates (mostly dolomite; green), magnetite (blue), and sulphides (mostly pyrrhotite; yellow) of a dry-polished section of the Ryugu particle C0068 (adapted from Ito et al., 2022, licensed under CC BY 4.0). **(b)** Grain size and shape analysis of pyrrhotite grains from C0068. Grains used for the evaluation are highlighted in light blue, and the fitted ellipses are shown in black. Fits corresponding to multiple grains falsely detected as a single grain due to close proximity were manually removed (marked in red). Smaller grains not included in the evaluation are shown in blue.

Fig. 1b illustrates the analysis of effective grain radii and shapes for pyrrhotite in the Ryugu particle C0068 as an example. The effective radius is defined as the radius of a circle with the same area as the respective grain. Grain contours were first extracted from the image, and the enclosed pixels were summed to obtain the grain area (highlighted in light blue and blue). Each contour was then fitted with an ellipse (shown in black) whose area closely matches the pixel-derived value. Small grains[1] for which this was not possible (highlighted in blue) were excluded from the subsequent analysis. In addition, detections where overlapping grains were identified as a single grain were manually removed from the dataset (marked in red). Of the remaining fits, only those differing by less than 50 % (25 %) in area from the grain contour area for grains with an area of less (more) than 50 pixels were retained to ensure a reliable analysis. A more permissive threshold is applied to grains smaller than 50 pixels, as ellipse fitting becomes less stable for such small objects and can therefore produce larger relative deviations between the fitted ellipse and the measured grain area.

The grain shape is quantified using the aspect ratio, defined as the ratio of the major to the minor axis of the fitted ellipse. Owing to the pixel resolution of the X-ray maps, the analysis of the three Ryugu particles is restricted to grains with effective radii larger than approximately 1–2 µm.

Fig. 2a shows the grain size distribution of the pyrrhotite grains extracted from Fig. 1b. Although the effective grain radii are derived from the projected grain area, a cumulative volume distribution is shown; the reason for this is discussed later in this section. It can be seen that 50 % of the pyrrhotite volume from grains larger than 1–2 µm. is contained in grains ranging approximately 15–30 µm.

Fig. 2b shows the cumulative grain volume and number distributions as a function of the grain aspect ratio. Pyrrhotite grains range from nearly spherical shapes with aspect ratios close to one to elongated, rod-like grains with aspect ratios of up to eight. As the cumulative volume and number distributions are relatively similar, the grain shape appears to depend at most weakly on grain size within the analysed size range.

[1] Small grains refers to connected regions of pixels whose outer boundary can be represented by less than five pixels.

3.2.2. Simulant material grain size and shape distributions

As described in Section 2, the aim here is to reproduce the grain size and shape distributions of the individual Ryugu components as closely as possible. Since the simulant production methods described in Section 4 do not lead to further grain breakage or dissolution, the distributions presented in this section represent the characteristic grain distributions in the simulants.

To compare the grain size and shape distributions of the simulant components used in this study with those of particles returned from asteroid Ryugu, the grain size distributions of the individual simulant components were determined using laser diffraction analysis (LDA) and backscattered electron (BSE) imaging as complementary methods, while BSE images were additionally used to characterise grain shapes. LDA measurements were performed with a *HELOS/KR + Quixel* laser diffraction instrument from *Sympatec* at the Institute of Geotechnology and Mineral Resources, Clausthal University of Technology.

In the LDA method, the grains are dispersed in a suspension and illuminated by a laser beam. The resulting diffraction pattern produced by light scattering is used to determine the cross-sectional area of each grain, which is then approximated by a circle to yield an effective grain radius. Using a multi-element detector, particles are sampled from multiple angles at high acquisition rates, resulting in volume-derived effective radii. The used laser diffraction instrument resolves effective grain radii from below 1 µm up to more than 1.5 mm. (Di Stefano et al., 2010; *Sympatec*, *Helos | R-Series | Laser Diffraction*, Technical Specifications, 20 Feb 2026)

For the BSE imaging analysis, grains were embedded in epoxy resin and prepared as polished thin sections. The analysis follows the same evaluation scheme as applied to the X-ray maps of the Ryugu particles (area-derived effective radii and aspect ratios) and is limited to grains larger than approximately 1 µm, similar to the X-ray mapping analysis.

For the thermal and mechanical properties of rocks or simulants composed of such grains, it is particularly important how smaller grains fill the voids between larger grains, thereby increasing both the number and total area of grain–grain contacts within the sample (Roquier, 2024; Johnson et al., 1971; Sakatani et al., 2017; Haack et al., 2020). For this reason, cumulative volume distributions of grain sizes and shapes are considered in the following.

Fig. 2a shows the size distributions of the simulant pyrite grains derived from the LDA method and BSE images. The generally acceptable agreement between both methods for the pyrite grains and the other simulant components (Fig. B.1 in Appendix B) supports the conversion from area-weighted to volume-weighted distributions by assuming the projected area-to-volume relationship of a sphere for both BSE imaging and X-ray mapping data.

Nevertheless, some deviations are observed. Grain size distributions derived from LDA are slightly shifted towards larger sizes compared to those from BSE imaging, although the overall size ranges are similar. This difference may result from shielding of small grains during laser diffraction measurements, over-segmentation in BSE image analysis, or grain splitting during thin-section preparation. Differences in the maximum effective grain radius are also evident. For dolomite and pyrite, a few grains identified in BSE images are nearly twice as large as the largest grains detected by LDA, while the mixed simulant material shows a slightly smaller maximum grain size than the coal component, likely due to partial crushing of weak coal grains during mixing.

Grain size and shape distributions of the simulant components derived from BSE imaging show overall good agreement with those of the Ryugu components obtained from X-ray mapping (e.g. pyrite/pyrrhotite

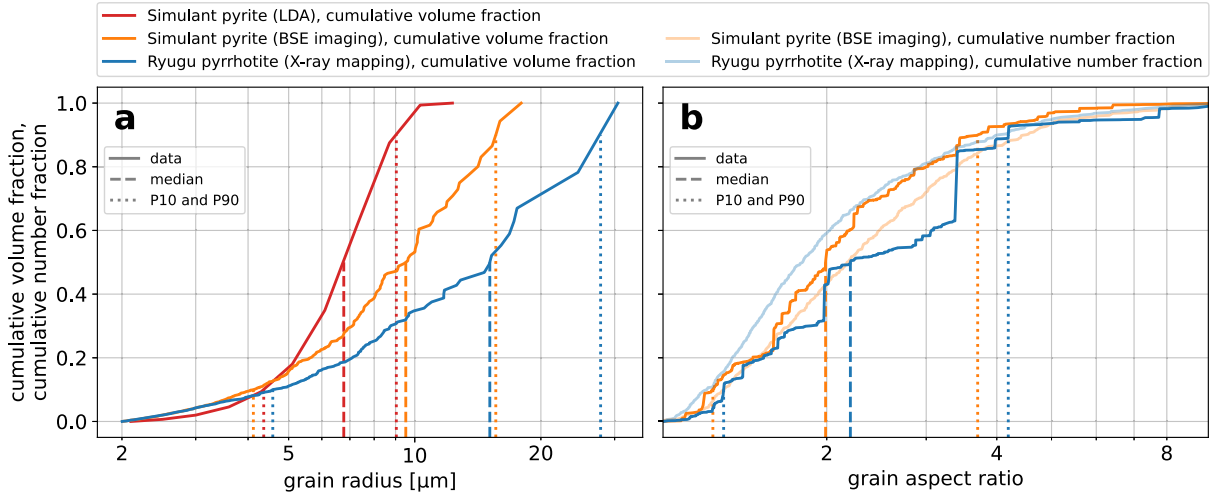

Fig. 2. **(a)** Cumulative volume distribution of pyrrhotite grains in Ryugu particles (X-ray mapping) compared to pyrite grains in the simulant mixture (LDA and BSE imaging) as a function of the effective grain radius. Marked are as well the median and the 10 % (P10) and 90 % (P90) percentiles. **(b)** Cumulative volume and number distribution of the pyrrhotite grains (X-ray mapping) compared to the pyrite grains (BSE imaging) as a function of the grain aspect ratio. Marked are as well the median and the 10 % (P10) and 90 % (P90) percentiles.

in Fig. 2; Table 2). The median effective grain radii and corresponding distribution widths[2] of the Ryugu components (pyrrhotite, magnetite, and dolomite) differ from those of the corresponding simulant components (pyrite, magnetite, and dolomite) by less than a factor of two, while the median aspect ratios and their distribution widths differ by less than 30 %. As noted above for the Ryugu pyrrhotite grains, comparisons of cumulative number and volume distributions as a function of aspect ratio indicate that the aspect ratio does not strongly depend on grain size within the evaluated size ranges for either the simulant or Ryugu components (Fig. B.2 in Appendix B).

Organic grains in the Ryugu particles predominantly occur in the nanometre to micrometre range, whereas the hard brown coal grains used as an organic simulant are at least one order of magnitude larger (Tachibana, 2023; Leroux et al., 2023; Lauretta et al., 2024). Similarly, the phyllosilicate matrix in Ryugu particles, primarily composed of serpentine and saponite, consists of fine submicrometre grains as well as larger clusters of several tens to hundreds of micrometres (Ito et al., 2022), whereas the phyllosilicates in the simulant are dominated by grains of a few to several tens of micrometres, lacking a true fine-grained matrix. Because finer grains in chondrites provide a mechanically strengthening foundation (Fujii et al., 1981) and, as shown in Section 5.4, build a reinforcing network in the high-porosity simulants (Section 4.1), this discrepancy may lead to comparatively lower-strength simulants. A more detailed discussion follows in Section 6.2.

Grain size and shape distributions of the individual simulant components together with the analysed Ryugu components are provided in Figs. B.1 and B.2 in Appendix B.

4. Simulant production

The simulants produced in this study are based on the dust mixture described in the previous section and are designed to reproduce boulders with porosities ranging from about 40 % to over 70 %, as inferred from observations made by the Hayabusa2 spacecraft on the surface of asteroid Ryugu (Sakatani et al., 2021). When the dust mixture is loosely poured into a container and gently shaken to allow the particles to settle, the packing reaches a bulk porosity (hereafter porosity) of approximately (67 ± 2) %. Simulants with lower porosities can be obtained by compressing a certain amount of the dry dust mixture, whereas the production of competent simulants[3] with higher porosities from the pure dry dust mixture is technically feasible only with considerable effort, if at all, as shown for ∼1.5 µm spherical SiO_2 particles (Blum and Schräpler, 2004).

A more effective method to produce high-porosity samples is freeze-drying, where the dust is mixed with water, frozen, and subsequently degassed by sublimation of the ice. Freeze-drying is a widely used technique with a broad range of applications (Deville, 2013). Similar studies have also been conducted, particularly for the production of porous lunar regolith simulants, but were unable to produce samples with porosities exceeding 70 % without the addition of bonding agents that were sufficiently competent for further analyses (Borella et al., 2023; Hossain and Bullard, 2025; Ricardo et al., 2023).

Several procedures of the freezing process were tested and are summarised in Appendix C. These preliminary trials did not result in useable samples due to various issues. The method described in the following section, however, was developed as a reliable approach to produce frozen samples with satisfactory homogeneity and a well-distributed pore structure (described in more detail in Section 5.2.2).

All produced simulants are cylinders with a diameter of 50 mm and a height of approximately 20 mm.

The following subsection gives a detailed overview of the production of high-porosity simulants (60 % to 80 %). The second subsection describes the production of low-porosity simulants (45 % to 60 %).

4.1. Production of high porosity simulants

The production of highly porous and homogeneous simulants used in this work is based on the freezing of a dust–water mixture and the subsequent sublimation of the ice in a vacuum environment, so that only the porous dust structure remains. First of all, the dust mixture described in Section 3.1.2 is mixed with distilled water in a mass ratio of

$$\frac{m_\mathrm{d}}{m_{\mathrm{H_2O}}} = \frac{\rho_\mathrm{d}}{\rho_{\mathrm{H_2O}}} \frac{1-\psi}{\psi} \tag{1}$$

[2] The distribution width is defined as the range between the 10 % and 90 % percentiles.

[3] Competent refers to optically thick, and strong enough to bear its own weight under earth gravity.

Table 2
Grain size and shape distributions from polished sections of Ryugu particles A0058-C1001, C0002-C1001 and C0068 (Yokoyama et al., 2023; Ito et al., 2022) and the simulant components used in this work. Data from plots in Fig. B.1 and B.2 in Appendix B.

Component	Volume-weighted effective radius [μm]		Volume-weighted aspect ratio	
	Median	distribution width	Median	distribution width
Ryugu components (X-ray mapping)				
Pyrrhotite	15	5–28	2.2	1.3–4.2
Magnetite	4	3–7	1.5	1.1–2.3
Dolomite	16	5–25	1.5	1.3–2.0
Simulant components (BSE imaging)				
Chrysotile (Serp.)	8	3–13	1.8	1.4–2.8
Beidellite (Sap.)	24	8–32	1.6	1.2–2.5
Pyrite	10	4–16	2.0	1.3–3.7
Magnetite	7	3–11	1.9	1.4–3.3
Dolomite	11	4–20	1.4	1.3–2.7
Hard brown coal	40	8–60	1.5	1.3–2.1
Simulant Mixture	17	6–42	1.8	1.3–2.4
Simulant components (LDA)				
Chrysotile (Serp.)	10	5–16	–	–
Beidellite (Sap.)	26	15–39	–	–
Pyrite	7	4–9	–	–
Magnetite	6	4–8	–	–
Dolomite	7	5–10	–	–
Hard brown coal	35	20–53	–	–
Simulant Mixture	21	11–30	–	–

with the dust mass m_d, the water mass m_{H_2O}, the dust density ρ_d, the water density ρ_{H_2O} and the desired final simulant bulk porosity ψ.

As the final bulk porosity of the simulant results from the drying of the frozen dust–water mixture, the densities of both dust and water at the final freezing temperature (~120–170 K) have to be used. This temperature was measured using Pt1000 sensors and corresponds to the temperature of the sample holder (described below) at the moment when the dust–water mixture was fully frozen. The water density at 120–170 K is $\rho_{H_2O} \approx 930\,\mathrm{kg\,m^{-3}}$ (Carnahan et al., 2021). The dust density $\rho_d \approx 2600\,\mathrm{kg\,m^{-3}}$ can be taken from Table 1 as it is not significantly influenced by the temperature.

The dust–water mixture and the sample holder depicted in Fig. 3a,b, which is later used to freeze the mixture, are pre-cooled to around 4 °C in a refrigerator to reduce the subsequent temperature gradient during freezing.

The sample holder consists of a PTFE cylinder with an inner diameter of 50 mm, an outer diameter of 80 mm, and a height of 20 mm, combined with a stainless-steel plate 70 mm in diameter and 3 mm thick that is screwed to the bottom of the PTFE cylinder. Two Pt1000 sensors are mounted on the stainless-steel plate and on the PTFE cylinder to monitor the temperature evolution.

The dust–water mixture is then filled into the sample holder and placed on an aluminium block that is in direct contact with a liquid nitrogen reservoir (Fig. 3a,b). The mixture is cooled for approximately 10 min, with an average cooling rate of ~15 K min^{-1} from the stainless-steel plate at the bottom and ~10 K min^{-1} from the PTFE sidewall. PTFE is used for the cylinder to promote preferential freezing from bottom to top, since stainless steel conducts heat roughly 60 times better (Nishikawara et al., 2014). Although aluminium would be even more effective, it is prone to corrosion over time and is therefore not used.

Once the dust–water mixture has frozen, the expansion of the water has formed a mound that rises from the edge to the centre at the top of the sample. To retain the desired shape of the simulant, the mound is removed with a random orbital sander. The frozen dust–water mixture is then extracted from the sample holder and placed inside a vacuum chamber for approximately two days at room temperature until a final pressure of 0.5 Pa is reached.

Finally, the dry, and highly porous simulant can be extricated from the vacuum chamber and used for further analysis (Fig. 3c).

4.2. Production of low porosity simulants

The production of more compact simulants in this work was achieved by confined compression of the dry dust mixture described in Section 3.1.2. The required dust mass

$$m_d = \rho_d V_c (1 - \psi) \tag{2}$$

is calculated based on the target bulk porosity ψ, the dust density $\rho_d \approx 2600\,\mathrm{kg\,m^{-3}}$ (Table 1), and the intended sample volume $V_c = \pi r_c^2 h_c$, where $r_c = 25$ mm and $h_c = 20$ mm are radius and height of the final simulant.

The dust is filled into a stainless-steel compression mould (Fig. 3d,e) and manually stirred using 400 μm diameter needles to deagglomerate the mixture. The mould consists of a square stainless-steel block with a base of 70 × 70 mm and a height of 60 mm, containing a central cylindrical cavity with a diameter of 50 mm. The cavity is closed at the bottom by a screwed stainless-steel plate with a thickness of 10 mm.

Compression is carried out by pressing a brass piston into the cavity and tightening the upper stainless steel plate with screws until it rests on the mould. With a piston height of 40 mm, this procedure yields a final sample height of approximately 20 mm.

If a noticeable elastic relaxation occurs after loosening the screws and releasing the pressure, resulting in an increased sample height, an additional compression step is performed to enable particle rearrangement and further densification. The compact simulant can then be removed from the mould and used for further analyses (Fig. 3f).

Achieving porosities lower than 45 % would require compression pressures exceeding the capabilities of the experimental setup used here (e.g., by employing a hydraulic press) and is not considered further in this study.

5. Structural characterisation

Following the description of simulant production in the previous section, the internal structure of the samples is examined in detail. Particular focus is placed on the microstructure, including spatial porosity variations and the overall density distribution, as well as on the nature of grain–grain contacts.

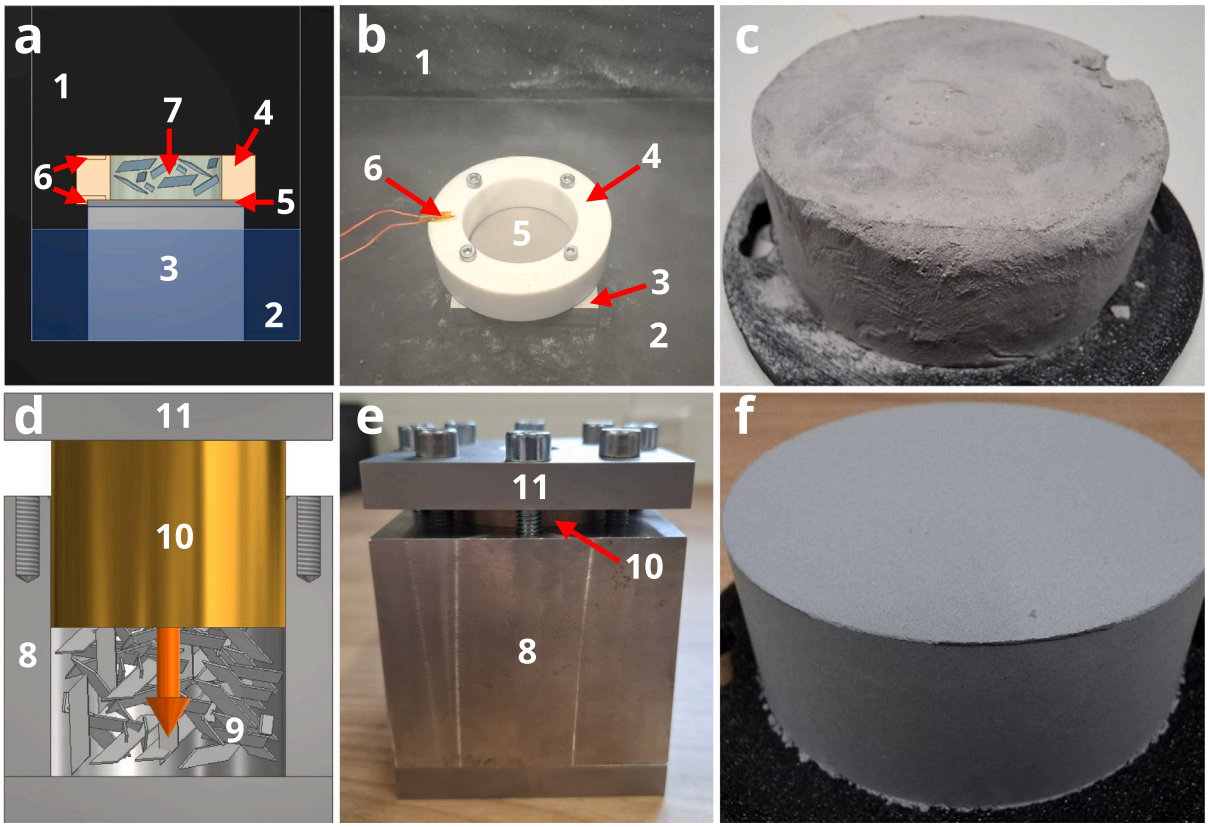

Fig. 3. **(a,b)** Setup for freezing the dust–water mixture, consisting of a Styrofoam box (1) containing a liquid nitrogen reservoir (2). Inside, an aluminium block (3) is placed with the sample holder on top, which consists of a PTFE cylinder (4) screwed to a stainless-steel plate (5). The cylinder includes two ports for Pt1000 temperature sensors (6) (one is shown in **(b)** as an example). The dust–water mixture (7) is filled into the cylinder. **(c)** Freeze-dried simulant sample with a porosity of 80 %. **(d,e)** Setup used for the compression of dry dust. It consists of a stainless-steel block with a cylindrical cavity and a screwed stainless-steel bottom plate (8), the dry dust (9) filled into the mould, a brass cylinder (10) used to compress the dust, and a stainless-steel plate (11) placed on top. **(f)** Compressed simulant sample with a porosity of 45 %.

As outlined in Section 2 and explained in Sections 5.1 and 5.3, the primary objective of this work is to produce samples that are as homogeneous as possible while establishing grain–grain contacts with the highest achievable stability.

The microstructure of the simulants was analysed via micro-tomographic analysis (μCT) using a *Comet YXLON FF85* from *Comet YXLON GmbH* at the Museum für Naturkunde Berlin. Since no complete CT datasets are currently available for analysing the Ryugu particles, an initial assessment and comparison are instead based on a qualitative evaluation of BSE images.

At present, no methodology has been established to quantitatively determine grain–grain contacts or the forces acting between grains. The analysis of the Ryugu particles is based on transmission electron microscopy (TEM) images and existing literature. For the simulant samples, BSE images are used to provide an initial qualitative assessment of the grain–grain contacts.

5.1. Ryugu particles microstructure

For a general assessment of the microstructure, three representative BSE images of Ryugu particles with effective radii of approximately 750 µm, 400 µm, and 100 µm are considered here (Fig. 4). Fig. 4a shows the largest of these particles, which exhibits a largely homogeneous density distribution.[4] A red circle marks one of the largest heterogeneous regions, likely attributed to magnetite or an Fe-sulphide, with an effective radius of approximately 30 µm. Apart from this feature, a finer-scale mixture of brighter and darker regions can be observed throughout the particle. In addition, several rounded, very dark regions are present, which are likely to represent pores. A representative example is marked by a blue circle and has an effective radius of approximately 15 µm.

Fig. 4b shows the second-largest particle. Here, a dense region is circled in red with an effective radius of approximately 40 µm. In addition to these relatively uniformly bright areas, which can be interpreted as individual grains, larger regions with less uniform brightness can also be observed. These still differ in their overall brightness from the surrounding material, such as the darker, less dense region marked by a purple circle, with an effective radius of approximately 100 µm.

Beyond such small-scale heterogeneities, some particles also exhibit larger structural features, such as the approximately 200 µm long vein shown in Fig. 4c (yellow dashed rectangle). This feature appears to consist of smaller grains, likely magnetite or Fe-sulphides. In addition to heterogeneities on the scale of several tens to a few hundreds of micrometres, even larger heterogeneities in the submillimetre range have been reported in some particles (Nakamura et al., 2022). Furthermore, Tsuchiyama et al. (2024) report general density variations and

[4] As shown, for example, in Ito et al. (2022) for a BSE image of a Ryugu particle, the brightness correlates, to a first approximation, with the density of the different mineral phases considered here.

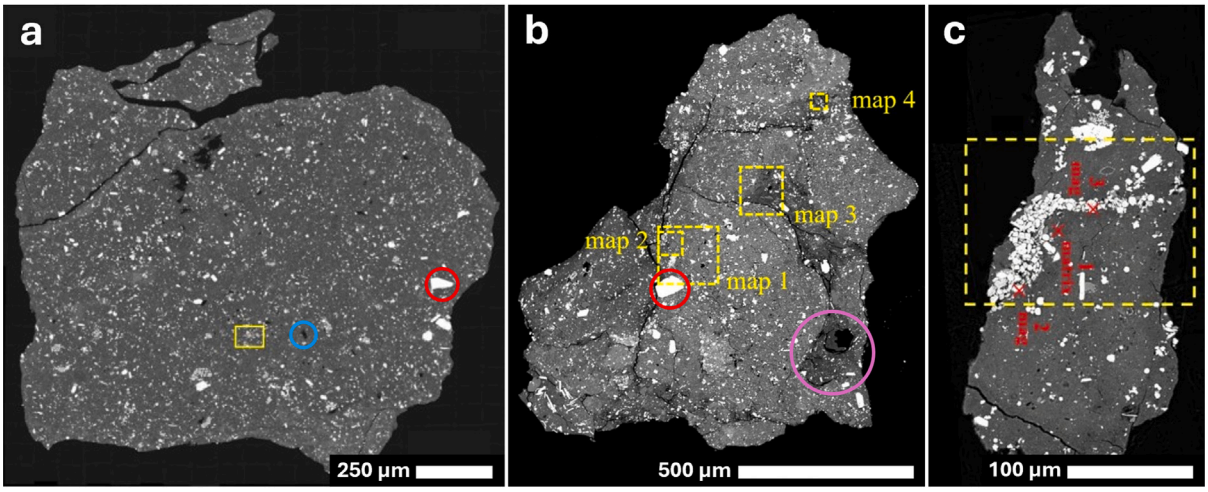

Fig. 4. BSE images of particles returned from Ryugu showing microstructural characteristics. **(a)** Polished section of particle C0014 (adapted from Tomioka et al., 2023, licensed under CC BY 4.0). The blue circle marks a larger, very dark area, most likely attributed to a pore, with an effective radius of approximately 15 µm, the red circle marks a dense material region, attributed to magnetite or an Fe-sulphide, with an effective radius of approximately 30 µm. **(b,c)** Polished sections of particles C0033-04 and C0033-01 (adapted from Bazi et al., 2022, licensed under CC BY 4.0). In **(b)**, the red circle marks a dense material region with an effective radius of approximately 40 µm, and the purple circle marks a less dense region with an effective radius of approximately 100 µm. In **(c)**, a dense vein approximately 200 µm in length is highlighted by a yellow dashed rectangle.

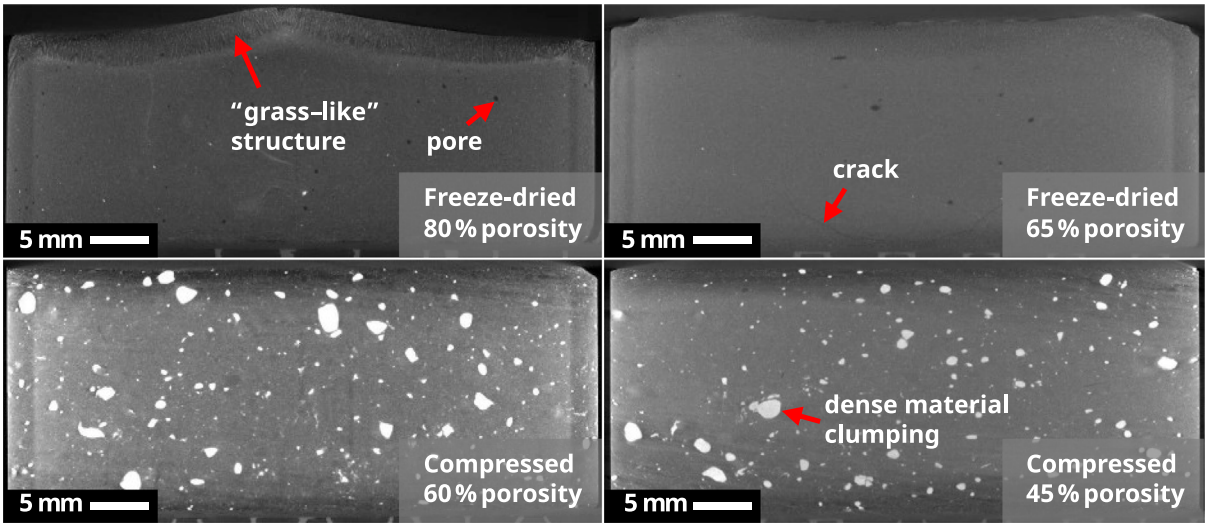

Fig. 5. Overview µCT cross-sections of representative samples produced by freeze-drying and compression, highlighting key features described in Sections 5.2.2–5.2.4.

thus heterogeneities among different Ryugu particles from the same sampling site.

Overall, large areas of relatively homogeneous structure are observed, containing isolated pores on the scale of individual grains. However, locally strongly heterogeneous regions on length scales exceeding 100 µm are also present. To provide a basis for further development, the aim for the simulants in this work is therefore to achieve heterogeneities below approximately 100 µm, which corresponds roughly to the diameter of the largest grains in the simulant material. Larger pores should likewise be largely absent.

As shown in Fig. 4, several cracks are also present in the Ryugu particles. However, reproducing such cracks is not an objective of this study and they are not targeted in the simulant development.

5.2. Simulant microstructure

µCT analyses were conducted on freeze-dried samples with nominal porosities of 80 % (sample IDs F80a and F80b), 65 % (F65a and F65b), and 60 % (F60a and F60b), as well as on compressed samples with porosities of 60 % (C60a and C60b) and 45 % (C45a and C45b). For each specimen, an overview scan covering the entire cylindrical volume was acquired at a spatial resolution of approximately 43 µm.

The µCT data were evaluated to address the following key aspects:

1. The existence of global radial or vertical density gradients.
2. The size and spatial distribution of pores within the sample.
3. The homogeneity of the material distribution within the sample.
4. The occurrence of structural defects, such as cracks.

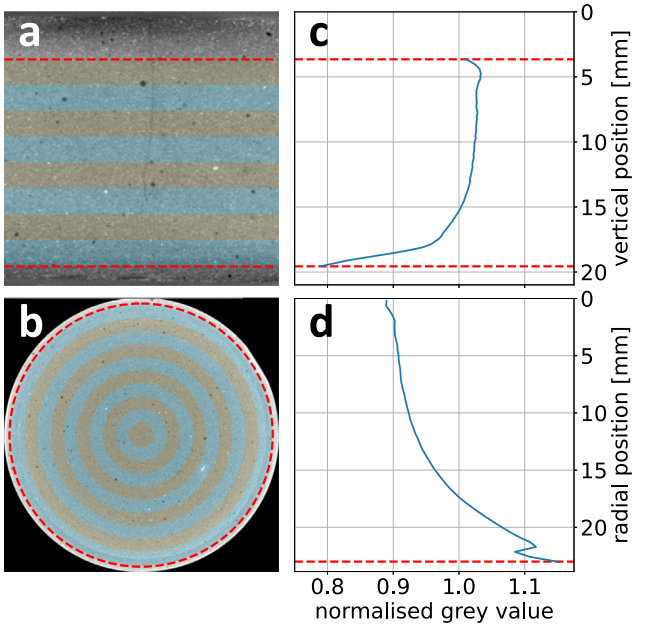

Fig. 6. Grey-value profiles of the freeze-dried sample F80b. **(a)** Vertical cross-section showing coloured bands used to average the density (visually exaggerated for clarity; 70 bands used in the analysis). The red outline marks the region used for analysis, and the vertical axis corresponds to **(c)**. **(b)** Horizontal cross-section with coloured rings used for averaging density (visually exaggerated for clarity; 50 bands used in the analysis). The red outline indicates the region considered for analysis. **(c)** Normalised grey values of the analysed sample region as function of the vertical position. **(d)** Normalised grey values of the analysed sample region as function of the radial distance from the sample central axis.

Representative cross-sections of freeze-dried and compressed samples reveal systematic structural differences between the production methods (Fig. 5). The compressed samples exhibit numerous regions of higher density, expressed by lighter grey values (Guntoro et al., 2019). These dense clumps are attributed to pyrite and magnetite accumulations and occur far less frequently in the freeze-dried samples. This observation indicates that mixing of the individual simulant components in the dry state is limited, whereas mixing in an aqueous environment leads to a significantly more homogeneous distribution. In the freeze-dried samples, the dust components are mixed on such fine spatial scales that the material largely appears uniform in the μCT slices.

In contrast, the freeze-dried samples contain numerous darker features (described in more detail in Section 5.2.2) with diameters exceeding approximately 50 μm, interpreted as macro-pores. Such macro-pores are much less abundant in the compressed samples. These must be distinguished from micro-pores, which represent the voids between individual grains and cannot be resolved in the μCT data. The combined contribution of micro- and macro-pores defines the porosity of the samples.

In Fig. 5, the freeze-dried sample with 80 % porosity additionally exhibits a central uplift originating from the freezing process, as described in Section 4.1. This excess material is typically removed afterwards to obtain a cylindrical geometry. For the present analysis, the uplift was removed only for the sample F80b (80 % porosity) in order to assess the influence of this post-processing step.

The freeze-dried samples F60a and F60b (60 % porosity) show a large number of internal cracks, as will be shown later in Fig. 8c in Section 5.2.4. Owing to this significant structural deficiency, they were excluded from further analysis and are not considered in the following evaluation.

5.2.1. Density gradients

Global density profiles reflect variations in porosity in the case of a homogeneously mixed material. Thus, the density profiles primarily indicate how well the methods described in Section 4 produce consistent porosities throughout an entire sample.

For the analysis, a slightly smaller cylindrical region was extracted from each sample (marked by the red lines in Fig. 6a,b), to remove fractures, cracks, and surface irregularities introduced during production or handling. To evaluate global vertical density gradients, each sample was subdivided into horizontal layers, each corresponding to a μCT slice, and the mean grey value per layer was computed as a proxy for density (Guntoro et al., 2019). These values were normalised to the volume of the layer and the global mean grey value of the corresponding sample and plotted against the vertical position (Fig. 6c). Global radial density gradients were assessed by subdividing samples into concentric rings around the central axis, computing the mean grey value per ring, normalising to the ring volume and then normalising to the global mean grey value of the sample (Fig. 6d).

The μCT grey values reflect the X-ray attenuation according to the Beer–Lambert law and depend on material density as well as other factors, such as the X-ray source spectrum (Guntoro et al., 2019). Thus, without further calibration, no direct correlation can be established between relative changes in grey value and changes in density that would imply proportionality between the two quantities. Nevertheless, a constant or only weakly varying grey-value distribution would indicate a comparatively homogeneous density within the sample. As samples were irradiated laterally, beam hardening (Brooks and Chiro, 1976) introduces artificial brightening from the centre to the edges, limiting the use of the radial profiles to qualitative comparisons between samples.

Fig. 6c shows the vertical grey-value profile of the freeze-dried sample F80b (80 % porosity) over an analysed height of ∼16 mm. The grey value increases slightly from the upper edge, remains rather constant (variation <3%) over a ∼11 mm central region and drops again to the lower edge by ∼15 %. The production method thus yields a relatively homogeneous vertical density distribution over roughly half the sample height. The radial grey-value profile in Fig. 6d reveals a ∼30 % increase up to ∼23 mm from the centre.

Similar results are observed for the other freeze-dried and compressed samples. However, the radial grey-value increase is notably higher in the compressed samples, reaching roughly 30–50 %. After correcting for beam hardening, this indicates a stronger radial density increase than in the freeze-dried samples. Minor kinks near the outer edges, present in all samples except C45a (45 % porosity), are scanning artifacts.

Vertical and radial grey-value profiles for all samples are provided in Figs. D.1–D.4 in Appendix D.

Overall, no conclusive explanation can be provided for the general vertical decrease of density near the top and bottom edges, or for a possible slight radial increase towards the outer regions. Although the influence of these gradients cannot be quantified in detail here, they are inconsistent with the level of homogeneity targeted in Section 5.1. A more quantitative characterisation of these gradients, and potentially an optimisation of the production methods, could be addressed in future work.

5.2.2. Size and spatial distribution of macro-pores

Freeze-dried samples contain abundant macro-pores (hereafter pores) whereas such features are rare in compressed samples. The following analysis therefore focuses on pores in the freeze-dried samples only. These pores reduce the volume occupied by solid material and thereby the porosity of the remaining material relative to the porosity intended during production.

Pores were segmented in all μCT slices of the freeze-dried samples using a grey-value threshold defined as the minimum grey value in each slice plus 60 % of the difference between the minimum and median grey values. Their two-dimensional contours were identified (Fig. 7a)

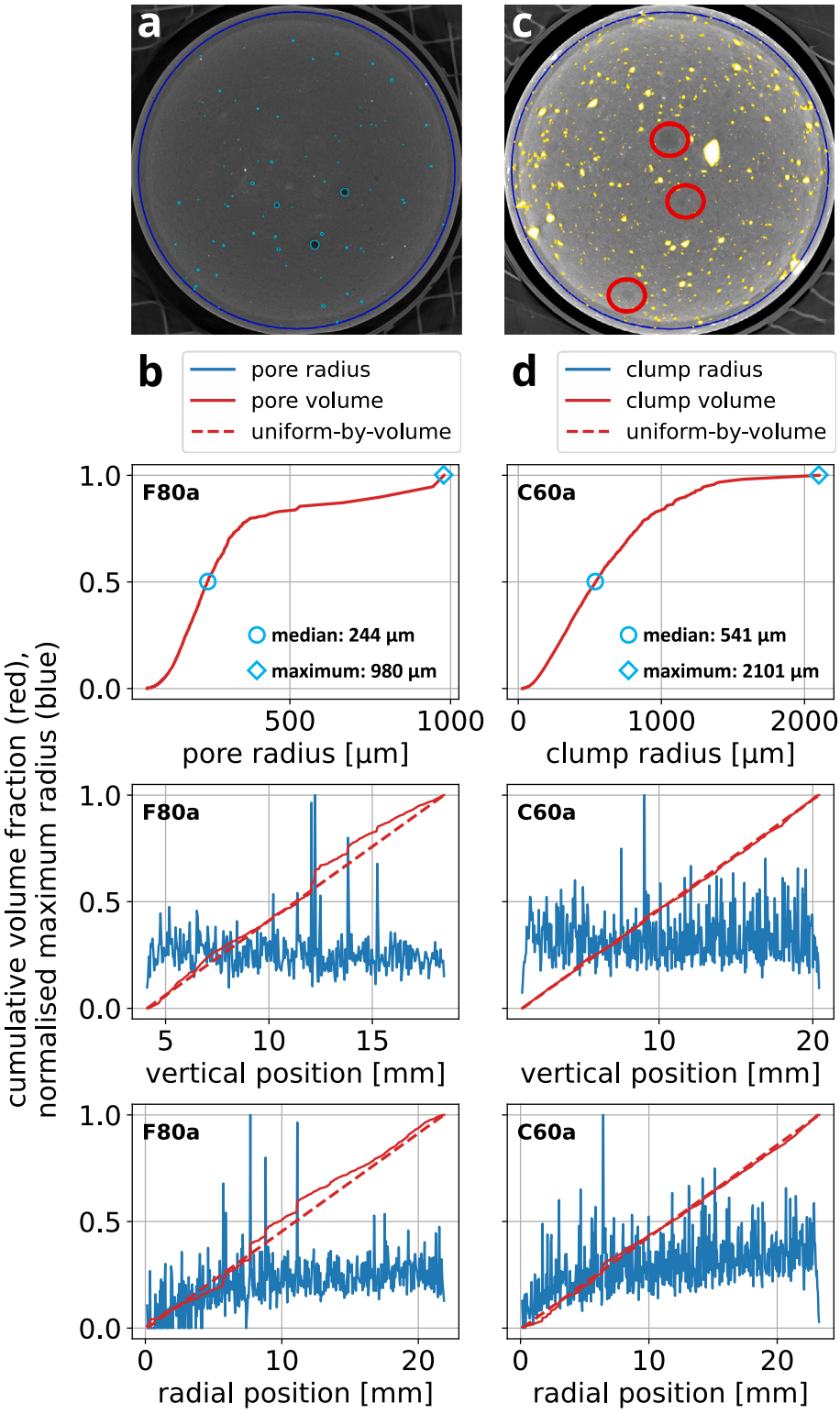

Fig. 7. Size distribution of pores and dense clumps in freeze-dried and compressed samples. **(a,c)** Example µCT slices of freeze-dried sample F80a **(a)** and compressed sample C60a **(c)**. Segmented pores **(a)** and dense clumps **(c)** are shown as light blue and yellow contours within the analysed circular region (dark blue ring). Exemplary low-density regions in the compressed sample **(c)** are indicated by red circles. **(b,d)** Global cumulative volume distribution of pores **(b)** and dense clumps **(d)** as function of their effective radius, as well as cumulative volume distributions and maximum effective radii (normalised to the global maximum) as functions of vertical position and radial distance from the sample central axis, with a uniform-by-volume distribution for comparison.

and matched in consecutive slices to reconstruct the three-dimensional pore volume. Assuming spherical pore shapes, effective radii were derived from the reconstructed volumes. To avoid misidentifying edge fractures as pores, a radially and vertically reduced cylindrical volume was extracted from each sample for analysis, similar to the extraction described in Fig. 6a,b.

For interpretation, the cumulative volume distribution of the pores is analysed as a function of their effective radius. Fig. 7b exemplarily shows for sample F80a (80 % porosity) a strongly concave distribution with a median effective pore radius of ~240 µm and a maximum effective pore radius of ~1000 µm.

In addition, the analysed sample volume is subdivided vertically into cylindrical intervals and radially into concentric ring-shaped intervals, similar to the subdivision shown in Fig. 6a,b. Within each interval, the pore volume, normalised to the respective interval volume, and the maximum effective pore radius, normalised to the global maximum of the sample, are evaluated as functions of vertical position and radial distance. Fig. 7b shows for sample F80a (80 % porosity) a largely homogeneous spatial distribution of pores, with no clear vertical or radial trends in total pore volume. Likewise, no systematic variation of maximum pore size with height is observed. A slight radial trend is detectable, with smaller pores preferably in the sample's centre (below 5–10 mm from the central axis). A direct link between this behaviour and the production process described in Section 4.1 cannot be established. The small kinks in the cumulative volume distributions as functions of vertical and radial position, representing minor deviations from the uniform-by-volume distribution, result from peaks in the maximum pore size, as the total pore volume is dominated by the larger pores.

While the radial and vertical pore distributions are similar for the other freeze-dried samples, the global cumulative volume distributions of the samples with 65 % porosity are less concave than those of the 80 % porosity samples and show a median effective pore radius of approximately 600 µm.

Corresponding results for all freeze-dried samples are provided in Figs. E.1 and E.3 in Appendix E.

It should be noted that smaller pores, typically with effective radii below 100 µm, were likely underdetected due to insufficient contrast. To account for this limitation, the measured pore volume is conservatively doubled. Even under this assumption, pores contribute less than 3 % of the total sample volume. This corresponds to corrected porosities of approximately 79.4 % and 63.9 %, remaining close to the intended 80 % and 65 %. For comparison, a 10 % reduction in effective sample volume would yield corrected porosities of about 78 % and 61 %, respectively.

In the freeze-dried samples, pores are present that are significantly larger than those targeted in Section 5.1. However, these pores account for only a very small fraction of the total volume and can therefore be tolerated at the current stage of development.

5.2.3. Homogeneity of material distribution

As described before, the dust components in the freeze-dried samples are mixed so thoroughly that no material inhomogeneities are visible in the µCT slices, except for a few minor regions. In contrast, the compressed samples exhibit numerous larger areas where the denser components, probably pyrite and magnetite, occur in clumps. In addition to these dense clumps, several regions of slightly lower density are observed (Fig. 7c), likely corresponding to the less dense coal. The remaining components have very similar densities (Table 1), so clustering of these materials cannot be resolved by µCT. Such inhomogeneities reduce the interaction between individual components of the dust mixture, causing the macroscopic properties of the sample to result more from the sum of the individual components than from the mixture as a whole, and to be subject to stronger local variations at the scale of the inhomogeneities.

Due to their easy detectability, dense clumps in the compressed samples are used as a proxy for the homogeneity of the material distribution and are analysed similarly to the pores.

The global cumulative volume distributions as illustrated in Fig. 7d for sample C60a (60 % porosity) follow a trend similar to that of the pores, with a concave shape lying between those of the 80 % and 65 % porosity samples. While the median effective clump radii are similar to the median effective pore radii, ranging from about 350–650 µm, the maximum effective clump radius is more than twice as large as the maximum effective pore radius.

The vertical and radial distributions of the dense clumps are, similar to the pores, relatively homogeneous across the samples. No clear trend is apparent in the vertical distribution of clump sizes, except for a sharp decrease near the top and bottom edges, whereas in the radial distributions the maximum clump size generally increases outward before dropping sharply near the outer edge. These edge effects are likely artificial, possibly caused by the cylindrical cropping applied for the analysis, analogous to the pore evaluation. But no conclusive explanation can be provided for the observed radial gradient of maximum clump size related to the production method described in Section 4.2.

The corresponding data for all compressed samples are provided in Figs. E.2 and E.4 in Appendix E.

The dense clumps detected in sample C45b (45 % porosity) represent roughly 3 % of the sample volume, and about 6 % in the other compressed samples. As the pores, some smaller dense clumps (<100 µm) are not captured by the algorithm, suggesting that the actual volume fraction is slightly higher, conservatively estimated to increase by 1 %. Considering that all compressed samples contain approximately 9 % of denser material (magnetite and pyrite; Table 1), this indicates that roughly one-third to two-thirds of the dense material is finely mixed with the remaining powder.

The dry-pressed samples contain heterogeneous structures (clumps) on length scales that are significantly larger than those observed in Ryugu particles and those required in Section 5.1. Although, similar to the pores, these features account for only a relatively small fraction of the total sample volume, they incorporate a substantial portion of the denser material and thus noticeably affect the mixing ratio of the remaining part of the sample. To meet the requirements outlined in Section 5.1 in a satisfactory manner, further optimisation of the procedure will be necessary in future work.

5.2.4. Structural defects

Structural defects are here defined as features that cannot be classified within the three previously described categories: pores, material inhomogeneities, and other density gradients.

In the freeze-dried samples, two main types of defects are observed. The first is a "grass-like" structure in the upper region of the sample, consisting of fine, groove-like channels extending vertically from the layer in which they originate (Fig. 8a–c). The second type comprises fine to pronounced cracks (Fig. 8b–d). The "grass" is particularly pronounced in samples with high porosity (80 %) and becomes much weaker in samples with lower porosity (65 %) until it is no longer visible in samples with 60 % porosity (Fig. 8a–d). In contrast, cracks are nearly absent in highly porous samples (80 %) but increase in size and frequency with decreasing porosity (Fig. 8a–d).

The precise origin of the "grass" remains unclear, but it is associated with the freezing process of the dust–water mixture, as most of this region is removed in the sample F80b (80 % porosity) due to the removal of the central uplift after freezing (Fig. 8c). It may also be linked to lamellar structures observed in freeze-dried samples produced by other methods (Appendix C), resulting in a layer of higher porosity and reduced mechanical strength. Larger cracks in lower-porosity samples likely arise from compression and relaxation during sample preparation. The highly viscous dust–water mixture is spread into the mould with a spoon, inducing slight compression, and relaxes after the spoon is removed. Cracks can form in the sticky mass during this relaxation, become filled with water, and subsequently freeze. During drying, the ice sublimates, leaving the cracks behind. Finer vertical cracks, also present in high-porosity samples, may result from

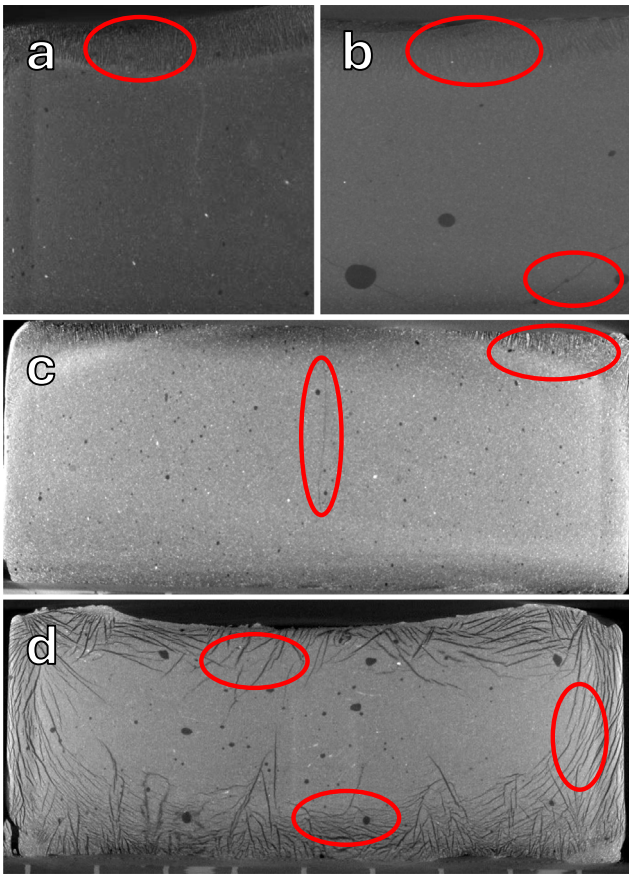

Fig. 8. Structural defects in freeze-dried samples. **(a)** µCT slice of sample F80a (80 % porosity) showing a "grass-like" region at the top of the sample (highlighted in red). **(b)** µCT slice of sample F65b (65 % porosity) with a "grass-like" region at the top and a crack at the bottom highlighted in red. **(c)** µCT slice of sample F80b (80 % porosity) showing a fine vertical crack and a "grass-like" region at the top of the sample near the radial outer edges (highlighted in red), absent from the centre. **(d)** µCT slice of sample F60a (60 % porosity) showing multiple cracks throughout the sample (highlighted in red).

mechanical vibrations during transport. While the exact origin of these cracks cannot be conclusively determined, they nevertheless weaken the overall sample structure.

In the compressed samples, no structural anomalies beyond those already classified in the previous subsections were observed.

5.3. Ryugu particles grain–grain contacts

The nature of grain–grain contacts in Ryugu particles is a key factor controlling several material properties, including bulk mechanical strength. High-resolution transmission electron microscopy (TEM) images (Fig. 9) reveal fine phyllosilicate (FPh) networks that embed and connect coarser grains (Fig. 9a), as well as intergrowths between different phyllosilicate phases within the FPh (Fig. 9b). These intergrowths establish connections at much smaller length scales and in a much more intimate manner than would be expected from simple van der Waals contacts in a granular packing (cf. Section 5.4).

Such intergrowth structures in boulders on the surface of Ryugu formed under specific conditions linked to the aqueous alteration of silicates such as olivine into phyllosilicates such as serpentine (Tomioka et al., 2023). On Earth, comparable structures can only be produced under specific conditions such as elevated temperatures and pressures or in aqueous environments combined with additional components at elevated temperatures, typically requiring long reaction times of up to several hundred days (Whitney, 1983; Serra et al., 2025).

Since such a procedure would require a considerable amount of experimental work and is currently incompatible with the methods for the simulant production described in Section 4, this study considers the grain–grain contacts to be defined by the chosen production method and subsequently analyses them in order to identify possible approaches for achieving highly stable contacts.

5.4. Simulant grain–grain contacts

In this study, simulants produced by the two different methods, as described in Section 4, are investigated. While the grain–grain contacts of samples produced with the same method but different porosities cannot be distinguished qualitatively, clear differences are observed between samples produced by these different methods. Therefore, a dry-compressed sample and a freeze-dried sample, both with porosities of 60 %, are compared in the following.

Fig. 10a shows two BSE images of a vertical cross section of the same freeze-dried sample with 60 % porosity. In general, finer grains seem to preferentially attach to larger ones and form bridge-like structures between them (marked by red ellipses), resulting in a network-like structure. This leads to larger total contact areas between grains and thus to an increased mechanical strength of the sample (Johnson et al., 1971; Haack et al., 2020).

A very different case is observed in Fig. 10b, which shows two BSE images of a vertical cross section of the same compressed sample with 60 % porosity. Here, both fine and coarse grains are distributed relatively homogeneously. At several locations, marked by red circles, coarse grains approach each other closely or even touch, but form contacts only at a few discrete points. This results in comparatively small contact areas and, consequently, a relatively low mechanical strength of the sample (Johnson et al., 1971; Haack et al., 2020).

A possible explanation for the different character of the grain–grain contacts lies in the mixing of the dust with water during the production of the freeze-dried samples. In the aqueous environment, the grains have higher mobility and can rearrange more freely. When two grains come into contact, they can attach to each other and reduce their combined surface area, thereby reaching a more energetically favourable state (Ignashova et al., 2023; German, 1996). The strength of such grain–grain contacts depends on the amount of energy released during this process.

Because smaller grains generally have a higher surface-to-volume ratio than larger ones, they preferentially attach to larger grains: the small grains lose a relatively large fraction of their surface area, while the surface area of the large grains increases only slightly in relative terms. The formation of the pronounced network-like structure observed in Fig. 10b, however, cannot be explained by this effect alone. The system is dynamic: grains can move within the liquid for several minutes before freezing, but the process may have been interrupted before an optimal energetic configuration was reached (Deville, 2013). Furthermore, the polar OH groups of the phyllosilicates, in combination with the irregular grain shapes, could promote strong hydrogen bonds compared to otherwise weak Van der Waals interactions. This could further reduce the system energy and may favour the development of the observed network-like structure.

6. Discussion

The aim of this work is to help close a gap in our understanding of the internal structure of boulders on the surfaces of C-type asteroids such as Ryugu by investigating a missing link between the thermal properties of meteorites found on Earth and the very low thermal inertia measured, for example, by Hayabusa2 on the surface of Ryugu.

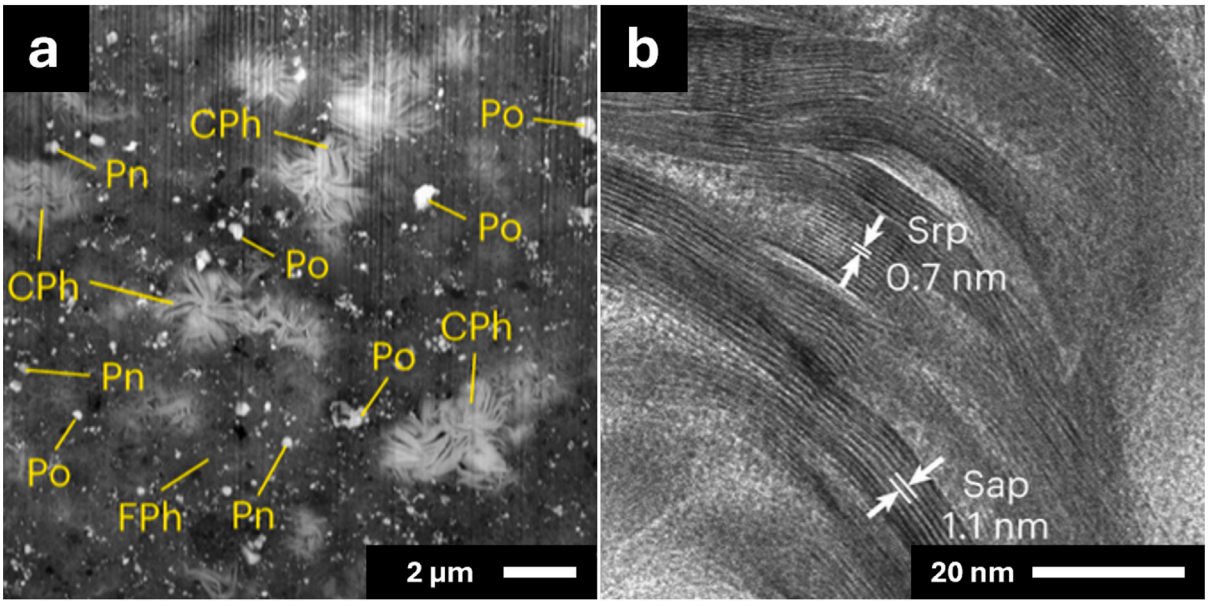

Fig. 9. TEM images of ultrathin sections of Ryugu particles (adapted from Tomioka et al., 2023, licensed under CC BY 4.0). **(a)** Dark-field scanning TEM image of a section of Ryugu particle C0068 showing coarse-grained phyllosilicates (CPh), pentlandite (Pn), and pyrrhotite (Po) embedded in a fine-grained phyllosilicate matrix (FPh). **(b)** Bright-field TEM image of a section of Ryugu particle A0037 showing nanometre-scale intergrowth of serpentine (Srp) and saponite (Sap).

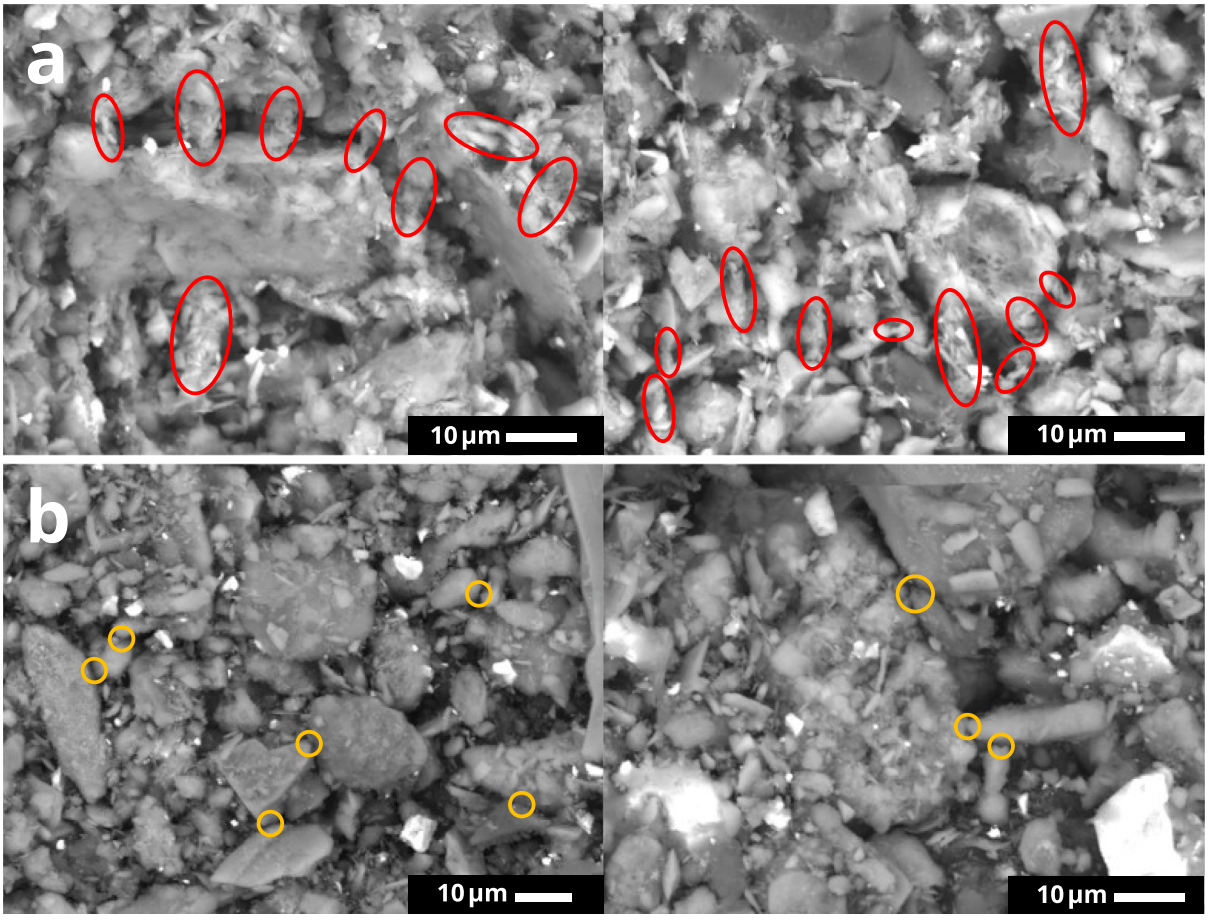

Fig. 10. BSE images of a vertical cross section of a **(a)** freeze-dried and **(b)** compressed sample with 60 % porosity. Red ellipses mark bridges of finer grains that have formed between coarser grains. Orange circles mark locations where coarse grains lie very close to each other or are already in contact.

To this end, this study describes methods for producing simulants with variable porosity, which is currently considered the main cause of the strong variations in thermal inertia. These simulants are intended to reproduce the thermal and mechanical properties of boulders on the surfaces of Ryugu-type asteroids as closely as possible, but not necessarily to replicate other properties, such as spectral or electrical characteristics. However, it must be stated from the beginning that a true reproduction of such boulders is impossible within realistic material and time constraints.

Nevertheless, valuable insights can be gained from analysing the simulants presented here and measuring, for example, their thermal and mechanical properties. They allow a deeper understanding of how variations in porosity, grain–grain contacts, and possibly also grain size distribution, grain shape distribution, or composition influence macroscopic parameters such as thermal conductivity and tensile strength, and how correlations between thermal and mechanical properties are mediated by the microscopic structure of the simulant.

To place the simulants of this work in the context of what is known about Ryugu's surface material, their properties are compared in the following subsections with respect to the five key aspects and objectives defined in Section 2: bulk composition, grain size distribution, grain shape distribution, microstructure, and grain–grain contacts. Furthermore, their implications for the thermal and mechanical properties of the simulants are discussed.

Finally, the present work is compared with alternative approaches for the production of simulants representing C-type asteroids such as Ryugu.

6.1. Composition

The main components of the Ryugu dust composition are summarised in Section 3.1.1. It is dominated by phyllosilicates, with smaller contributions from magnetite, pyrrhotite, dolomite, and organic matter. The material thermal conductivities of these phases are ~2–3 $\mathrm{W\,m^{-1}\,K^{-1}}$ for phyllosilicates, ~5 $\mathrm{W\,m^{-1}\,K^{-1}}$ for magnetite, ~5.5 $\mathrm{W\,m^{-1}\,K^{-1}}$ for dolomite, ~3.5–4.5 $\mathrm{W\,m^{-1}\,K^{-1}}$ for pyrrhotite, and between <0.1 and 1.5 $\mathrm{W\,m^{-1}\,K^{-1}}$ for organics/coal (Schön, 2011; Cermak and Rybach, 1982; Diment and Pratt, 1988). Except for the lower end of the organic values, all of these conductivities are of the same order of magnitude, so that no single component strongly dominates the bulk heat transport.

The dust mixture produced in this work follows the major Ryugu components as a baseline, but includes some modifications described in Section 3.1.2. Pyrrhotite was replaced by pyrite, and the complex organic fraction was represented by hard brown coal. The bulk thermal conductivity of hard brown coal is about 0.16 $\mathrm{W\,m^{-1}\,K^{-1}}$ (Kosowska-Golachowska et al., 2014), at the lower end of the range given above, whereas pyrite has a much higher conductivity of about 19–25 $\mathrm{W\,m^{-1}\,K^{-1}}$ (Schön, 2011; Cermak and Rybach, 1982; Diment and Pratt, 1988), roughly five times larger than that of pyrrhotite.

In addition to these intentional differences, contaminations were identified in several components of the dust mixture (Table A.1 in Appendix A), particularly in magnetite and dolomite. The dominant contaminant is crystalline quartz, whose literature density (2.65 $\mathrm{g\,cm^{-3}}$) is similar to that of dolomite (2.85 $\mathrm{g\,cm^{-3}}$) but only half that of magnetite (4.8 $\mathrm{g\,cm^{-3}}$). This likely explains the lower measured density of the magnetite powder (4.1 $\mathrm{g\,cm^{-3}}$, Table 1). In contrast, the reduced measured density of the pyrite powder (4.1 $\mathrm{g\,cm^{-3}}$, Table 1) compared to the literature value (5.0 $\mathrm{g\,cm^{-3}}$) cannot be explained by quartz contamination alone, as the contamination level is too low. However, no further analysis was conducted to explain this difference (Diment and Pratt, 1988).

The bulk thermal conductivity of crystalline quartz is about 6–10 $\mathrm{W\,m^{-1}\,K^{-1}}$ (Schön, 2011; Cermak and Rybach, 1982; Diment and Pratt, 1988), i.e. up to roughly three times higher than that of magnetite and dolomite.

Overall, differences between the Ryugu dust and the dust mixture used in this work do exist. However, since the combined volume fraction of pyrite and contaminating quartz is only about 10 vol.%, their influence on the bulk thermal conductivity of the mixture is expected to be of minor importance.

Henke et al. (2016) showed that the effective thermal conductivity of a rock without porosity (i.e., the bulk material thermal conductivity) composed of several components can be reasonably estimated using the Bruggeman mixing rule,

$$k_{\mathrm{eff,B}} = \left(\sum_{i=1}^{N} \frac{3 f_i}{2k_{\mathrm{eff,B}} + k_i} \right)^{-1} \tag{3}$$

where f_i denotes the volume fraction of component i and k_i its bulk thermal conductivity.

Using the component thermal conductivities given above, the volume fractions described in Table 1 together with the quartz contamination reported in Table A.1 (Appendix A), and assuming similar organics in Ryugu and in the simulant material, the bulk thermal conductivities of the two materials are estimated as $k_{\mathrm{eff,\,Ryugu}} \approx 2.0\text{–}2.6\,\mathrm{W\,m^{-1}\,K^{-1}}$ and $k_{\mathrm{eff,\,simulant}} \approx 2.2\text{–}2.8\,\mathrm{W\,m^{-1}\,K^{-1}}$.

As this difference is small, the effects of replacing pyrrhotite with pyrite and of quartz contamination on the effective bulk thermal conductivity can be considered negligible.

6.2. Size and shape distribution

The grain size and shape distributions of the simulant components are analysed in Section 3.2.2 and compared with those of Ryugu. For pyrrhotite, magnetite, and dolomite, good agreement is found, with differences within a factor of two for grain size and 30 % for aspect ratio. In contrast, significant discrepancies exist for the organic and phyllosilicate components: the simulant lacks a volume-dominating fraction of micrometre-sized phyllosilicates, and the organic grains are at least one order of magnitude larger than those in Ryugu. No quantitative comparison of grain shapes is possible for these components. These size and shape distributions primarily influence thermal and mechanical properties through their effect on minimum achievable porosity and the amount of grain contacts (Section 2).

Previous modelling studies have investigated the effects of grain shape and size distribution, including friction, on porosity and coordination number (Zhou et al., 2011; Oquendo-Patiño and Estrada, 2022). Ellipsoidal grains with aspect ratios similar to those of the simulant mixture (Table 2) tend to increase both minimum porosity and coordination number relative to spherical packings. Size distributions in sphere packings comparable to that of the simulant mixture (Fig. B.1 in Appendix B) decrease porosity and increase the network coordination number[5] compared to monodisperse systems, while the addition of finer grains leads to only minor further changes. Friction increases porosity and reduces the network coordination number. However, since the simulant consists of a polydisperse assemblage of rough, irregularly shaped grains, these effects cannot be directly combined or applied quantitatively. Although no comprehensive model captures all factors simultaneously, ongoing studies continue to improve our understanding of how grain-scale properties control macroscopic behaviour (Garcia et al., 2009; Zivithal et al., 2024; Carrasco et al., 2025).

[5] Oquendo-Patiño and Estrada (2022) define the network coordination number as the number of contacts per grain for grains forming the force-bearing network of the packing.

Nevertheless, considering only the discrepancies in the grain size distributions between the Ryugu and simulant components, the model of Oquendo-Patiño and Estrada (2022) suggests a slightly smaller minimum achievable porosity and larger amount of contacts. Accordingly, the simulants are expected to exhibit lower thermal conductivity and mechanical strength compared to the Ryugu particles.

6.3. Microstructure and grain–grain contacts

To compare the structural characteristics of Ryugu's surface boulders with the simulants produced in this study, it is first necessary to consider the processes that formed and modified these boulders.

Ryugu is a rubble-pile asteroid whose individual fragments reaccreted from the remains of a disrupted planetesimal parent body (Neumann et al., 2021). The original material of this disrupted parent body formed over millions of years (Hazen et al., 2021; Neumann et al., 2021) under physical and chemical conditions, such as pressure and temperature, that can no longer be fully reconstructed and were likely very complex. During this period, phyllosilicates such as serpentine and saponite formed through aqueous alteration of silicate minerals like olivine, pyroxene, and possibly amorphous materials (Neumann et al., 2021; Nakamura et al., 2022; Fujiya et al., 2023; Yamaguchi et al., 2023; McCain et al., 2023; Takano et al., 2024). These alteration processes not only led to the formation of new minerals but also to the development of bonds between adjacent grains, creating a mechanically strengthened foundation, the matrix (Noguchi et al., 2024).

In subsequent evolutionary stages, the surface material on the rubble-pile asteroid was further modified by space weathering processes, such as micrometeoroid impacts and cosmic irradiation, leading, for example, to chemical alteration, thermal fatigue, or the formation of structural defects, such as fractures and cracks (Kohout et al., 2014; Libourel et al., 2020; Molaro et al., 2017; Patzek et al., 2024).

As described in Section 5.1, the particles returned from Ryugu exhibit heterogeneous structures on different length scales. In some regions, the heterogeneity is limited to approximately the grain scale, whereas other regions show structures extending over several hundred micrometres. In addition, general heterogeneity has also been reported between different particles from the same sampling site. Pores, in contrast, are generally only observed on much smaller scales of several to several tens of micrometres. Based on these observations, the aim for the simulants was defined as achieving a material distribution that is as homogeneous as possible while containing pores that are as small as possible.

The freeze-dried simulants characterised in Section 5.2 indeed exhibit a largely homogeneous structure, in which no significant heterogeneous regions larger than approximately 100 μm were detected. The abundance of larger pores is likewise sufficiently low to only have a comparatively minor influence on the remaining structure.

In contrast, the dry-compressed simulants contain no major pores but consistently exhibit larger heterogeneous regions (clumps). These regions lead to a significantly lower fraction of denser minerals (magnetite and pyrite) in the remaining sample volume. Furthermore, they are significantly larger than the heterogeneous regions observed in the Ryugu particles described in Section 5.1. In contrast to the Ryugu particles, the dense clumps in the dry-compressed simulants are not merely enriched in denser material, but instead mostly consist of compact accumulations of dense material. However, this observation may also be influenced by the limited resolution of the μCT scans and should be investigated further in future work.

Overall, the freeze-dried simulants reproduce both the targeted microstructure and the microstructure observed in the investigated Ryugu particles more successfully than the dry-compressed simulants. The heterogeneous regions present in the dry-compressed samples are currently not suitable analogues for the heterogeneous structures observed in Ryugu material.

The "grass-like" regions observed in the freeze-dried samples, as described in Section 5.2.4, can be disregarded for this comparison, as they can be removed prior to further characterisation. Regarding the other type of structural defects, although the deliberate introduction of cracks, as observed in Ryugu particles (Section 5.1), was not within the scope of this study, Section 5.2.4 shows that such features can in principle be generated. However, whether these defects are structurally and morphologically comparable to those observed in Ryugu particles cannot be determined within the scope of this work.

Apart from this, a detailed analysis of the density distributions within the simulant samples is not yet possible with the currently available dataset and remains necessary for a complete assessment of the sample homogeneity and microstructure. Depending on the strength and extent of these gradients, achieving global homogeneity as defined in Sections 2 and 5.1 would require an optimisation of the described production methodologies.

Beyond global structural characteristics, BSE imaging provides insight into grain–grain interactions in both freeze-dried and compressed samples. In compressed samples, grain–grain contacts are generally weak, and larger grains are often connected by only a few small contact points. In freeze-dried samples, in contrast, finer particles aggregate and form bridges between larger grains, resulting in a more interconnected framework. Freeze-drying is thus the more suitable method for producing stable grain–grain contacts, as targeted in Section 5.3. The nature of the grain–grain contacts in freeze-dried samples is at least one step closer to the intergrown grain networks observed in Ryugu particles than those in the compressed samples.

A quantitative prediction of the thermal and mechanical consequences of these structural differences is not possible without an appropriate physical model. Nevertheless, qualitative assessments can be made based on pore-size distribution, crack occurrence, and grain–grain contact strength. The effects of the observed material inhomogeneities on thermal and mechanical properties cannot be reliably estimated currently and are therefore neglected in this discussion.

In general, larger pores and fractures reduce both mechanical stability and the efficiency of thermal transport (Shen and Rose, 2024; Schöpfer et al., 2009). In the freeze-dried samples, however, pores occupy only a small and relatively homogeneously distributed volume fraction, suggesting that sufficient grain contacts remain to sustain mechanical integrity and thermal transport; their overall influence is therefore likely minor. Cracks, in contrast, may significantly weaken thermal and mechanical properties even at small thicknesses, particularly if they are oriented perpendicular to the direction of heat flow or parallel to the direction of applied stress (Hamm et al., 2025). Such almost horizontal cracks occur primarily in freeze-dried samples with lower porosity and are rare in samples with porosities of 65 % and higher.

Conversely, strong grain–grain contacts enhance both thermal transport and mechanical strength (Johnson et al., 1971; Sakatani et al., 2017; Haack et al., 2020). Given the pronounced differences in grain contacts between compressed and freeze-dried samples, it is reasonable to expect that, when normalised to porosity, freeze-dried samples with porosities of 65 % and higher exhibit greater thermal conductivity and mechanical strength than their theoretical compressed counterparts.

Despite some shortcomings, such as the observed macropores, the freeze-dried simulants appear to match the objectives defined in Section 2 more closely than the dry-compressed simulants. They are also likely to exhibit higher thermal conductivity and mechanical strength under otherwise identical conditions.

6.4. Comparison with existing simulant production methods

As described in the introduction, several recipes for dust mixtures and production strategies for CI simulants, as well as simulants specifically designed for Ryugu, Bennu, or the potentially closely related Martian moon Phobos, have previously been proposed in the literature

(Hildebrand et al., 2015; Britt et al., 2019; Miyamoto et al., 2021; Miyamoto and Niihara, 2021; Wargnier et al., 2024). A commercially available dust mixture for CI simulants is also provided by *Space Resource Technologies* (*CI Carbonaceous Chondrite Simulant*; Britt et al., 2019). In the following, these previous approaches are compared with the simulant developed in this work in order to highlight the differences that motivated the present redevelopment.

Some differences exist between the composition of the simulant presented in this work (Table 1) and those proposed by Hildebrand et al. (2015), Britt et al. (2019), and Miyamoto et al. (2021). Hildebrand et al. (2015) described a composition consisting of 85 vol.% phyllosilicates, 10 vol.% magnetite, and 5 vol.% organics. In comparison to the simulant developed here, Fe-sulphides and carbonates are absent, whereas the magnetite content is considerably higher. Britt et al. (2019) proposed a mixture of approximately 66 wt.% phyllosilicates, 10 wt.% magnetite, 7 wt.% olivine, 7 wt.% Fe-sulphides, 5 wt.% organics and 5 wt.% ferrihydrite, thus additionally including olivine and ferrihydrite but without carbonates. Similarly, the composition reported by Miyamoto et al. (2021), consisting of approximately 61 wt.% phyllosilicates, 8 wt.% magnetite, 7 wt.% olivine, 9 wt.% Fe-sulphides, 10 wt.% carbonates, and 5 wt.% organics, also contains additional olivine. Overall, while the relative abundances of the major components are broadly comparable, differences remain in the specific mineral phases included. The extent to which these compositional differences affect the final thermal and mechanical properties of the simulant cannot be conclusively assessed within the scope of this work but could be investigated in future studies.

The decisive reason for developing a new fundamental dust mixture instead of relying on the commercially available solution from *Space Resource Technologies*, however, is the grain size distribution of the dust components. According to the manufacturer, 84 wt.% of the material lies within a grain size range of 70–10 000 µm (*Space Resource Technologies*, *CI Carbonaceous Chondrite Engineering Simulant*, Fact Sheet 003-15-001-0823, 03 Nov 2025), which is more than one order of magnitude coarser than the grain size distributions measured for the samples returned from Ryugu (Tachibana, 2023). In addition, the traceability of the grain size distributions of the individual components is limited. Miyamoto et al. (2021) and Wargnier et al. (2024) reported the use of powders finer than 100 µm and mixtures consisting of 80 vol.% grains between 50–100 µm and 20 vol.% grains smaller than 1 µm, respectively, for their Phobos simulants. These grain size ranges are therefore at least of a similar order of magnitude to those of the dust components used in this work (Table 2).

Apart from the differences in composition, various production methods for asteroid simulants have been proposed. The most commonly used approach involves dry mixing of the individual dust components, followed by the addition of a small amount of water. The mixture is then dried at room temperature or at elevated temperatures of up to 370 K in a furnace. The resulting solid block is subsequently crushed to produce a regolith simulant with a defined grain size distribution (Hildebrand et al., 2015; Britt et al., 2019; Miyamoto et al., 2021; Miyamoto and Niihara, 2021). In some cases, a binder such as sodium metasilicate is added to the dust–water mixture to increase the strength of the resulting block and regolith (Britt et al., 2019; Avdellidou et al., 2020). This approach enables the production of larger amounts of relatively consolidated material. However, Hildebrand et al. (2015), Avdellidou et al. (2020), and Miyamoto et al. (2021) report porosities between 26–41 %, which are significantly lower than the target values in this study.

A less complicated approach is presented by Wargnier et al. (2024), who propose crushing, sieving, and dry mixing terrestrial rocks whose composition should match the target composition in order to obtain a regolith simulant wit a desired grain size distribution. However, this method cannot produce a monolithic simulant composed of multiple minerals and is additionally constrained by its intrinsic porosity, which cannot be adjusted deliberately.

Alternatively, López-Oquendo et al. (2024) suggest dry compression of dust to produce dense pellets, similar to the dry compression method described in this work.

A more complex approach for producing highly porous Phobos simulants was proposed by Wargnier et al. (2025). They prepared a dilute aqueous suspension containing 1 wt.% dust and atomised it into a liquid nitrogen reservoir using an ultrasonic nebuliser in order to freeze it immediately. The mixture of liquid nitrogen and ice particles is stored in a freezer to remove the liquid nitrogen while preserving the ice structure. The ice particles are then sieved and deposited onto a sample holder. The sample is placed in a vacuum chamber and carefully heated to slowly sublimate the ice, leaving behind a dust structure with a porosity exceeding 80 %. However, a single run of the experiment yields only around 6 mg of highly porous material, making this approach too time-consuming and resource-intensive for the quantities required in this study.

Overall, several approaches have been proposed for the preparation of basic simulant dust mixtures for CI chondrites and Ryugu-type asteroids, as well as for the production of regolith or general surface material. However, due to discrepancies regarding composition and grain size, and due to limitations in the preparation of sufficiently large, highly porous samples, an alternative method was developed in this study.

7. Conclusion

In this work, a strategy was developed to produce simulants designed to reproduce the assumed porosity range of boulders on the surface of asteroid Ryugu, with the aim of improving our understanding of the exceptionally low thermal inertia measured there (Grott et al., 2019). Furthermore, the simulants are intended to support a more general investigation of how parameters such as porosity and grain–grain contacts affect the thermal and mechanical properties of chondritic materials.

The simulant material is based on a dust mixture derived from the composition of particles returned from Ryugu. Using backscattered electron (BSE) imaging and laser diffraction analysis of the simulant components, together with X-ray maps of Ryugu particles, the mineralogical composition as well as the grain size and shape distributions were compared between simulant and Ryugu material. There are considerable discrepancies between the simulants and the Ryugu particles. In terms of composition, the Fe-sulphide pyrrhotite present in the returned Ryugu particles was replaced by the stoichiometrically different Fe-sulphide pyrite in the simulant. Regarding size distribution, the nanometre- to micrometre-sized organic grains in Ryugu particles are at least an order of magnitude smaller than those in the simulant mixture. While the simulant phyllosilicates adequately cover the larger tens- to hundreds-of-micrometre grains observed in Ryugu particles, the abundant submicrometre grains found in Ryugu are almost entirely absent in the simulant. Their potential impacts on the thermal conductivity and mechanical strength of the simulants are discussed in this work but cannot be quantified with the currently available models. These discrepancies could be addressed by future improvements of the dust mixture.

By employing two different production methods, freeze-drying of a dust–water mixture and compression of the dry loose powder, artificial rocks with porosities ranging from about 45 % to 80 % were successfully produced and structurally characterised using micro-tomographic analysis and BSE imaging. For samples produced with the same method, variations in porosity lead to broadly similar internal structures. In contrast, pronounced structural differences were observed between the two production methods. Freeze-dried samples exhibit a more homogeneous mixing of components on small scales, but also contain larger pores and structural defects such as cracks, which are absent in compressed samples. Most importantly, freeze-dried samples show significantly better interconnected grains than compressed samples,

Table A.1
Contaminants of individual components were identified. In particular, significant amounts of quartz were detected, mainly in the magnetite and dolomite fractions, and minor contribution of silicates, Fe-Ti oxides and gypsum. These phases are not significantly water-soluble (Plyasunov and Zyubina, 2021; Yuan et al., 2019; Scholz and Kahlert, 2015; Colombani and Bert, 2007), which could otherwise affect the production of highly porous simulants, and are comparable to the primary components in terms of their grain size and grain shape distributions, as observed in SEM images.

Component	Formula[a]	Known contaminants	Contaminated Fraction [vol.%][b]
Chrysotile	$(Mg_{2.95}Fe_{0.04})Si_2O_5(OH)_4$	Quartz, Ilmenite	8
Beidellite	$(Na_{0.08}K_{0.74})(Mg_{0.15}Fe_{0.13})(Al_{2.64}Si_4O_{10})(OH)_{8.4}$	Quartz, Ilmenite	2
Pyrite	FeS_2	Quartz, Gypsum	3
Magnetite	Fe_3O_4	Quartz	30
Dolomite	$CaMg_{1.06}(CO_3)_2$	Feldspar, Quartz	48
Hard brown coal	not measured	Fe-Al-Silicates	3

[a] Omitting minor contaminations and trace elements (< 0.5 wt.%).

[b] Fraction from SEM image analysis as area of contaminant grains relative to the area of all grains. Following the Delesse principle, for a random section through a homogeneous and isotropic volume, the area fraction of a given component is equal to its volume fraction in the bulk sample (Weibel and Elias, 1967).

Table A.2
Simulant components from *Edelstein-Schleiferei und -Handlung Giovanni Petronio in Hamburg, Germany*, *Sigma-Aldrich/Merck* and *Kohlen Sparen Brennstoffhandel GmbH*. The montmorillonite from *Sigma-Aldrich* has been characterised as beidellite with electron microscopy.

Simulant component	Supplier	Product ID/Source
Chrysotile (Serpentine)	*Giovanni Petronio*	*MP 10223 Serpentin – Puder* ≤ 63 µm
Beidellite (Saponite)	*Sigma-Aldrich*	*Montmorillonite K 10* (catalog number 69866)
Pyrite	*Giovanni Petronio*	*MP 10187 Pyrit – Micropuder ca.* 5–10 µm
Magnetite	*Giovanni Petronio*	*MP 10140 Magnetit – Micropuder ca.* 5–10 µm
Dolomite	*Giovanni Petronio*	*MP 10077 Dolomit – Micropuder ca.* 5–10 µm
Hard brown coal	*Kohlen Sparen*	*Severoceskych Dolu mine d.s. (Chomutov)*

which is expected to result in higher mechanical strength and thermal conductivity. This may represent an intermediate structural state between weakly bound granular packings and the strongly intergrown grain networks observed in Ryugu particles and CI chondrites (Noguchi et al., 2024). A quantitative analysis of radial and vertical density gradients within the samples cannot be performed with the current dataset. However, such an analysis would provide a valuable tool to assess the quality of the simulant production methods in terms of reproducibility and representativeness of the bulk porosity, and could be addressed in a follow-up study.

Beyond their application to thermal and mechanical measurements that will be carried out next, the simulants presented in this work provide a versatile experimental basis for further studies, including impact experiments, sound speed measurements, and electrical property investigations. As such, they offer a valuable tool for advancing our understanding of the physical behaviour of highly porous chondritic materials relevant to primitive asteroids (Sakatani et al., 2021; Omura and Nakamura, 2021).

CRediT authorship contribution statement

Moritz Goldmann: Writing – original draft, Methodology, Investigation, Conceptualization. **Markus Patzek:** Writing – review & editing, Supervision, Investigation. **Ansgar Greshake:** Writing – review & editing, Funding acquisition. **Bhuvan Agrawal:** Writing – review & editing. **Jens Biele:** Writing – review & editing. **Jürgen Blum:** Writing – review & editing. **Dominik Dieter:** Writing – review & editing. **Matthias Grott:** Writing – review & editing, Funding acquisition. **Carsten Güttler:** Writing – review & editing, Supervision. **Jörg Knollenberg:** Writing – review & editing. **Bastian Gundlach:** Writing – review & editing, Supervision, Funding acquisition.

Declaration of competing interest

The authors declare the following financial interests/personal relationships which may be considered as potential competing interests: Moritz Goldmann reports statistical analysis was provided by Clausthal University of Technology. If there are other authors, they declare that they have no known competing financial interests or personal relationships that could have appeared to influence the work reported in this paper.

Acknowledgments

This work was carried out within the framework of the project "Thermal and Mechanical Properties of Carbonaceous Chondrites" funded by the Deutsche Forschungsgemeinschaft (DFG GU 1620/6-1 project number 493620659).

We gratefully acknowledge Jacob Fenner, Petra Sommer, Sarah Tuchtfeld, and Daniel Goldmann from the Institute of Geotechnology and Mineral Resources, Clausthal University of Technology, for providing the laser diffraction and helium pycnometry data of the dust used in this study, and Kristin Mahlow-Tillack from the Museum für Naturkunde Berlin for providing the micro-tomographic data of the produced simulants.

We further acknowledge Open Access funding enabled by Projekt DEAL

Appendix A. Simulant composition contamination

See Tables A.1 and A.2.

Appendix B. Ryugu and simulant component grain size and shape distributions

See Figs. B.1 and B.2.

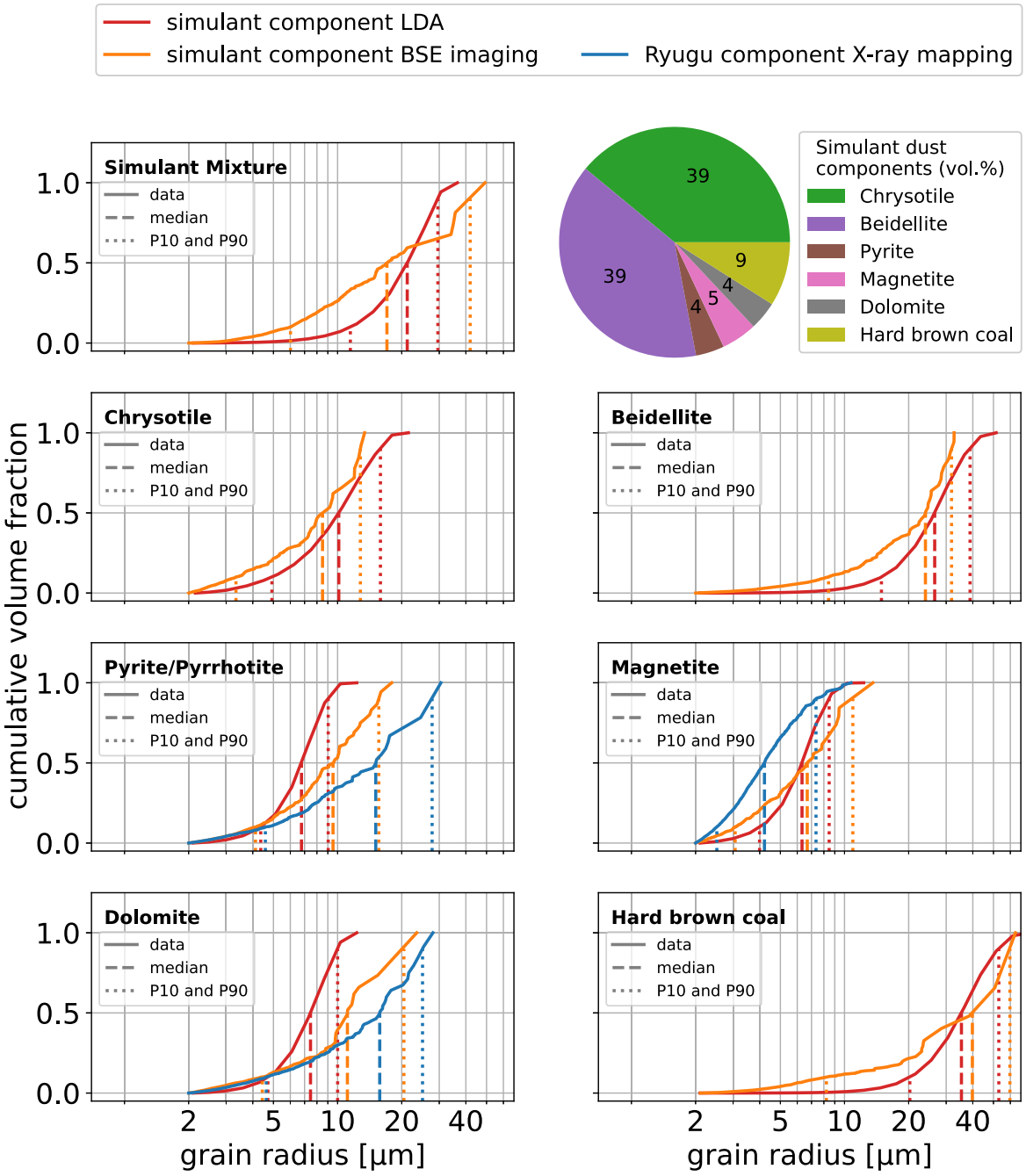

Fig. B.1. Cumulative volume distributions of grains in simulant mixture, simulant components and analysed Ryugu components, measured with different techniques as function of the effective grain radii. Marked are as well the median and the 10 % (P10) and 90 % (P90) percentiles.

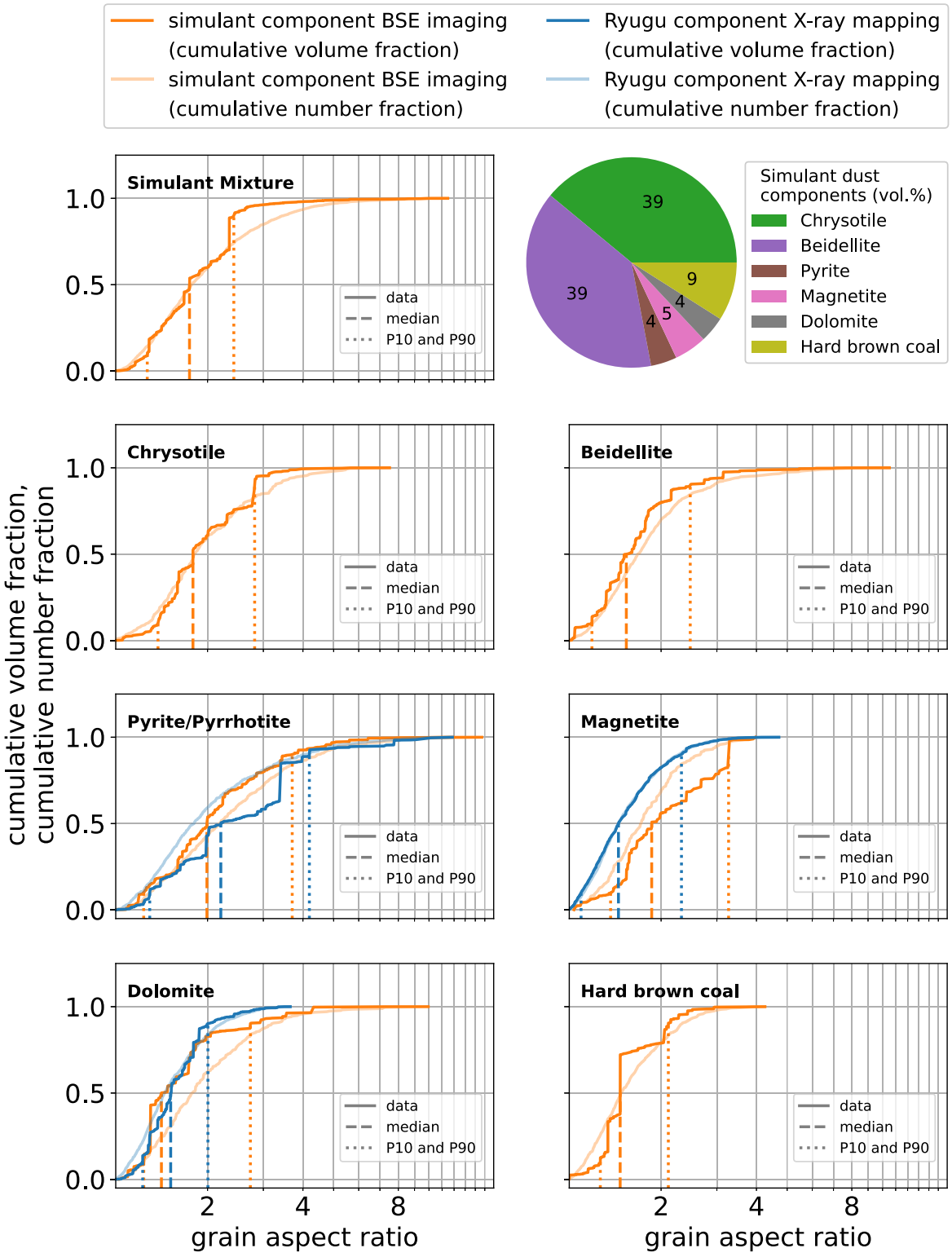

Fig. B.2. Cumulative volume and number distributions of grains in simulant mixture, simulant components and analysed Ryugu components, measured with different techniques as function of the grain aspect ratios. Marked are as well the median and the 10 % (P10) and 90 % (P90) percentiles.

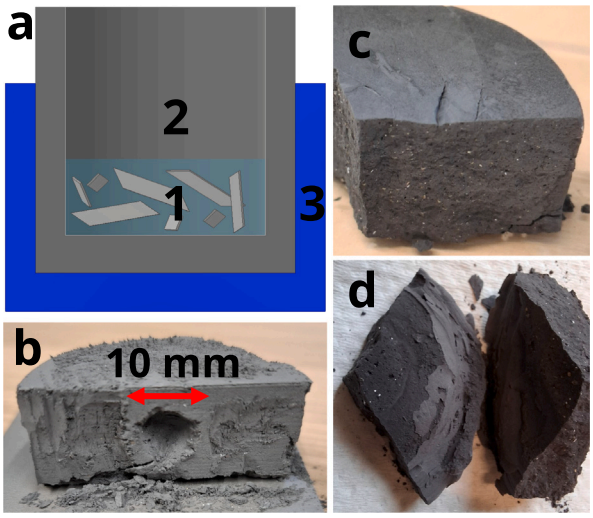

Fig. C.1. **(a)** Experimental setup for freezing a dust–water mixture (1) poured into an aluminium sample holder (2) placed in a liquid nitrogen (LN_2) reservoir (3). **(b)** Cut of a dried sample produced by rapid freezing, showing a central pore with a diameter of ∼10 mm. **(c)** Cut of a dried sample produced by layered freezing, which initially showed no visible cracks or layering, but **(d)** failed along a distinct internal plane under Earth gravity when rotated by 90°.

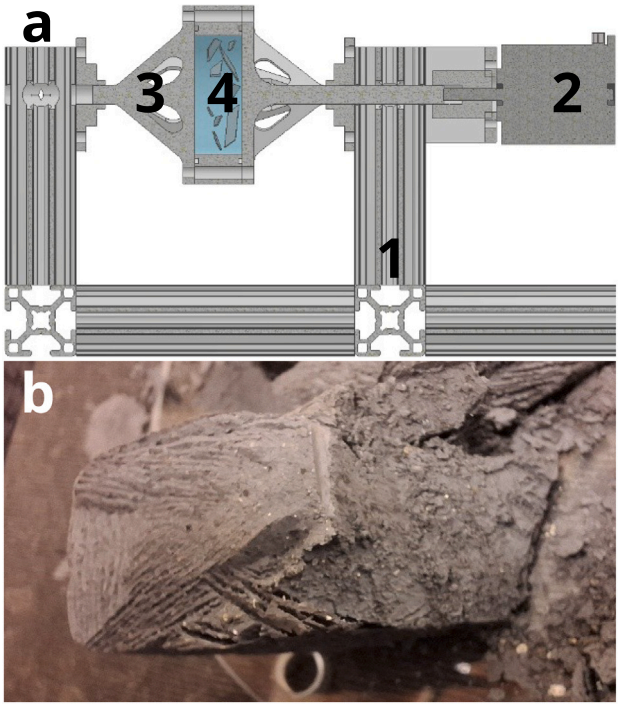

Fig. C.2. **(a)** Experimental setup, in which an aluminium strut frame (1) supports a stepper motor (2) that rotates a cylindrical sample holder (3) containing a dust–water mixture (4) inside a freezer. **(b)** Exemplary cut of a dried sample produced with the tumbler approach, showing lamellar features.

Appendix C. Simulant production failed versions

Before arriving at the method for producing highly porous samples described in Section 4.1, four different procedures for freezing the dust–water mixture were tested. All of these approaches were ultimately discarded because they led to structural deficiencies in the resulting samples. The drying procedure applied to the frozen samples, however, never changed.

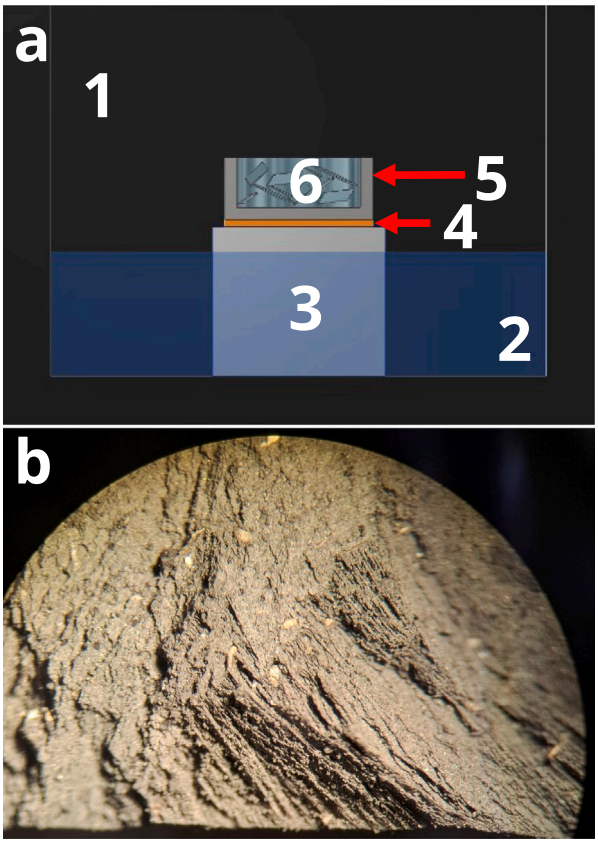

Fig. C.3. **(a)** Setup for freezing a dust–water mixture, showing a Styrofoam box (1) containing a liquid nitrogen reservoir (2). An aluminium block (3) is placed inside, topped with an insulating layer of variable thickness (4) and an aluminium sample holder (5), into which the dust–water mixture (7) is poured. **(b)** Exemplary cut of a dried sample produced with the insulated freezing approach, showing lamellar features similar to the tumbler approach.

For the rapid freezing method, the dust–water mixture was poured into an aluminium sample holder and directly immersed in liquid nitrogen (LN_2; Fig. C.1a). As freezing progressed from the outer boundaries towards the centre, intense bubbling occasionally occurred in the remaining unfrozen central region. This led to the entrapment of large gas bubbles, ranging from several millimetres to more than a centimetre in diameter, within the frozen sample. After subsequent drying, these bubbles resulted in a strongly inhomogeneous dust distribution (Fig. C.1b).

In the layered freezing method, the aluminium sample holder was precooled by direct contact with LN_2 before the dust–water mixture was added (Fig. C.1a). Once the holder had reached approximate thermal equilibrium, the mixture was poured in slowly and continuously, where it gradually froze. Due to the simultaneous filling and freezing process, internal layers formed within the sample. Although the layer boundaries are not clearly visible in the cut sample, their presence significantly reduced the contact strength between these layers (Fig. C.1c–d).

Using the tumbler approach, the dust–water mixture was poured into a sealed cylindrical container that was rotated about its principal axis at one revolution per minute in a freezer at −20 °C (Fig. C.2a). The resulting dried sample exhibited pronounced lamellar, sheet-like structures extending from the outer regions towards the centre (Fig. C.2b). These features strongly reduced the mechanical stability of the sample. They may have formed due to crystal growth in the dust–water mixture during freezing. If this is the case, the freezing rate would need to be increased to reduce the time available for crystallisation and thereby suppress crystal growth.

For the insulated freezing approach, both the dust–water mixture and the sample holder were precooled to approximately 4 °C in a freezer. The mixture was then poured into the holder, which was placed indirectly onto an aluminium block in direct contact with LN_2 (Fig. C.3a). An insulating layer of variable thickness (up to 20 mm) was inserted between the holder and the aluminium block. Similar to the tumbler approach, lamellar structures developed from the edges towards the centre, but they were considerably finer and less pronounced (Fig. C.3b). The lamellar pattern became weaker with decreasing insulation thickness.

Appendix D. Simulant density gradients

See Figs. D.1–D.4.

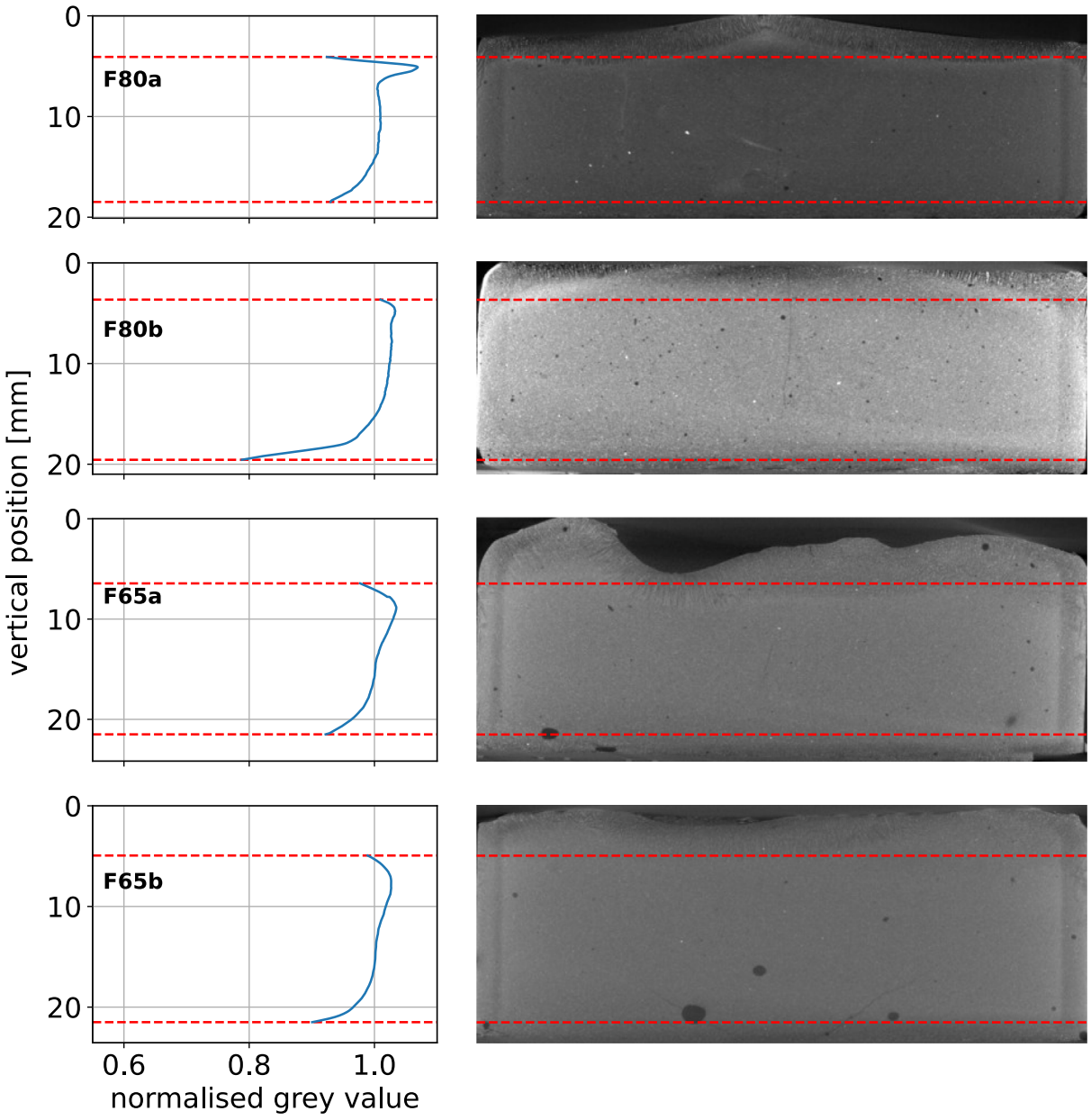

Fig. D.1. Normalised grey values as a function of the vertical position within the analysed region of the freeze-dried samples.

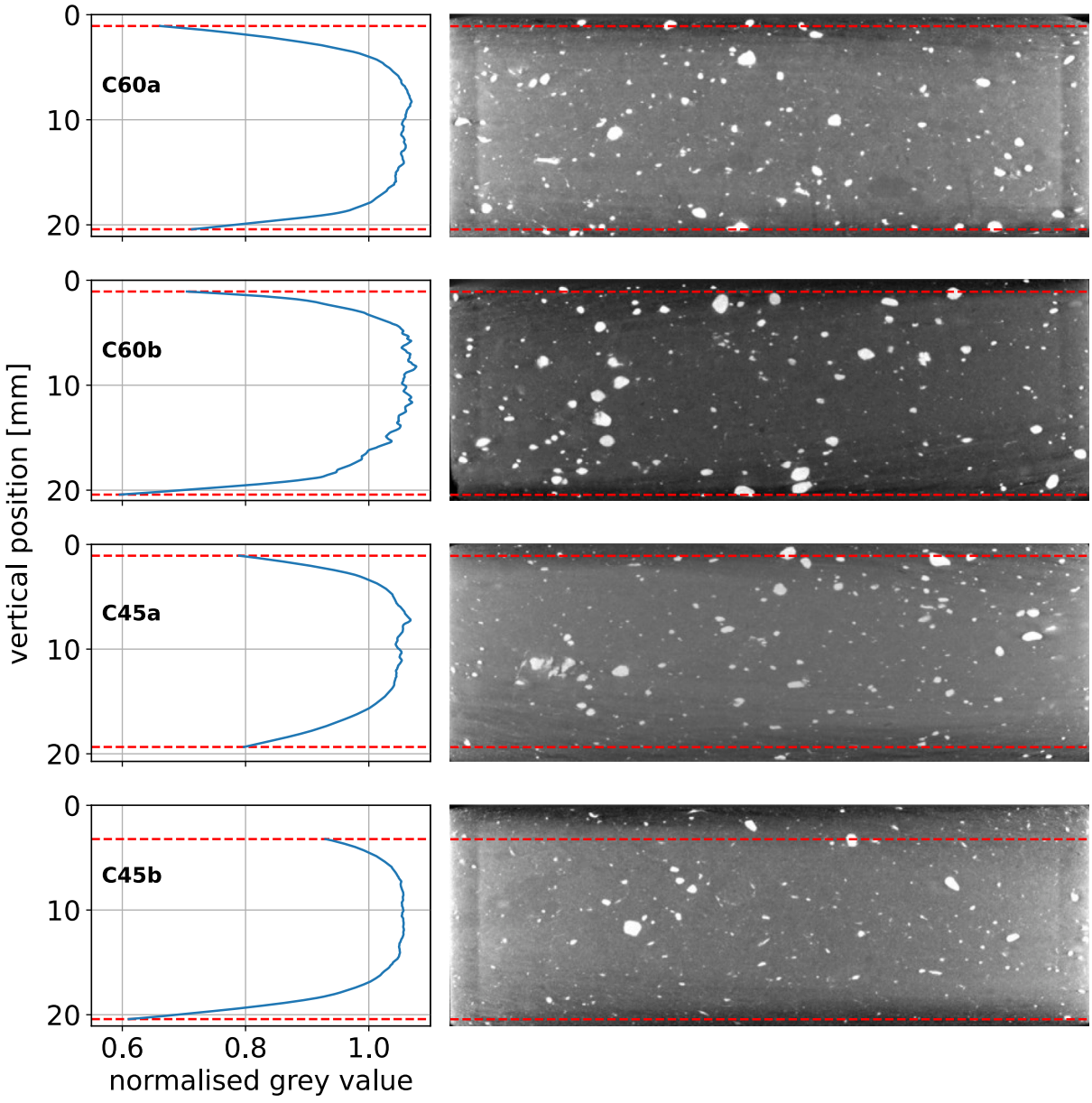

Fig. D.2. Normalised grey values as a function of the vertical position within the analysed region of the compressed samples.

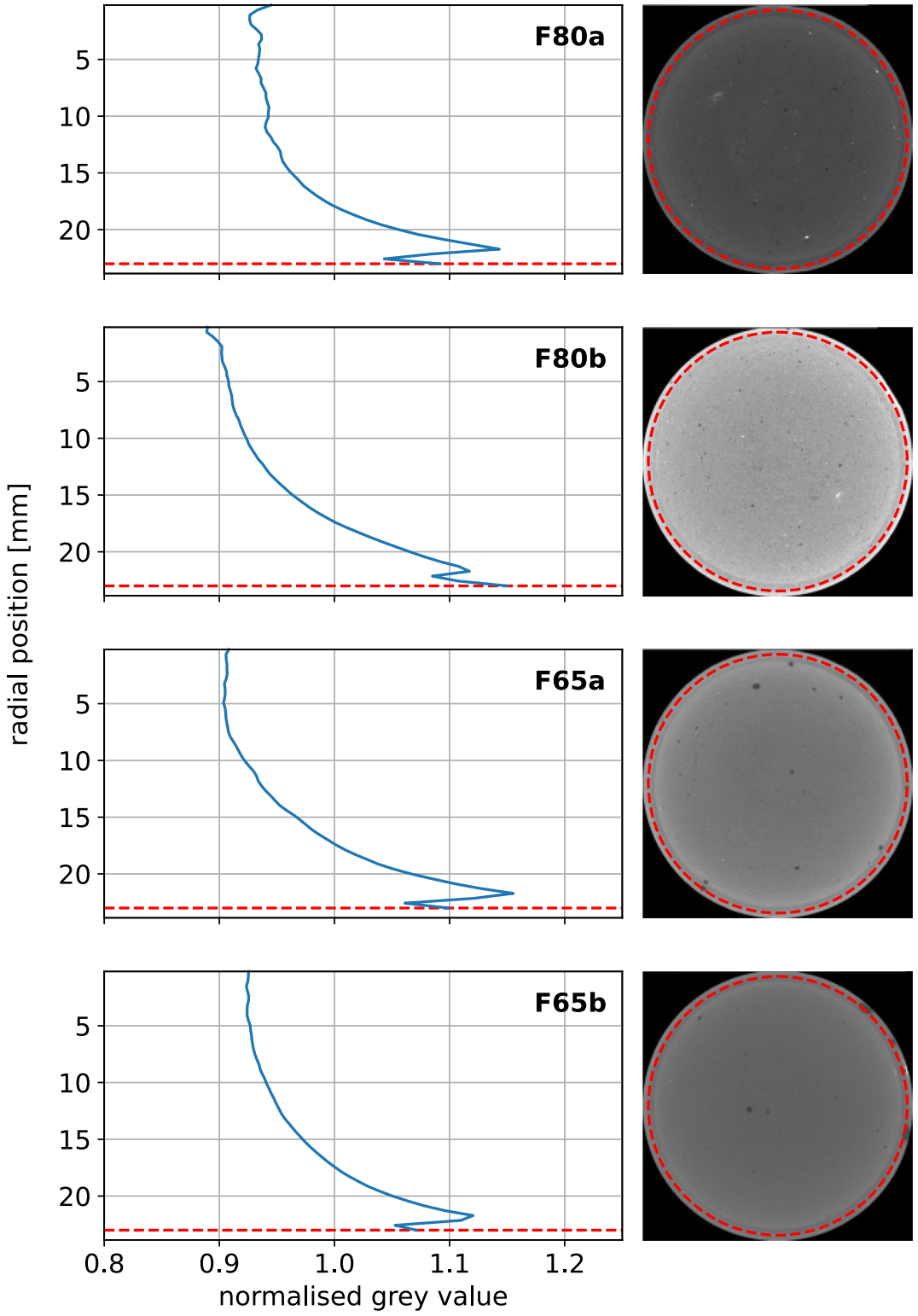

Fig. D.3. Normalised grey Values as a function of the radial distance from the sample central axis within the analysed region of the freeze-dried samples.

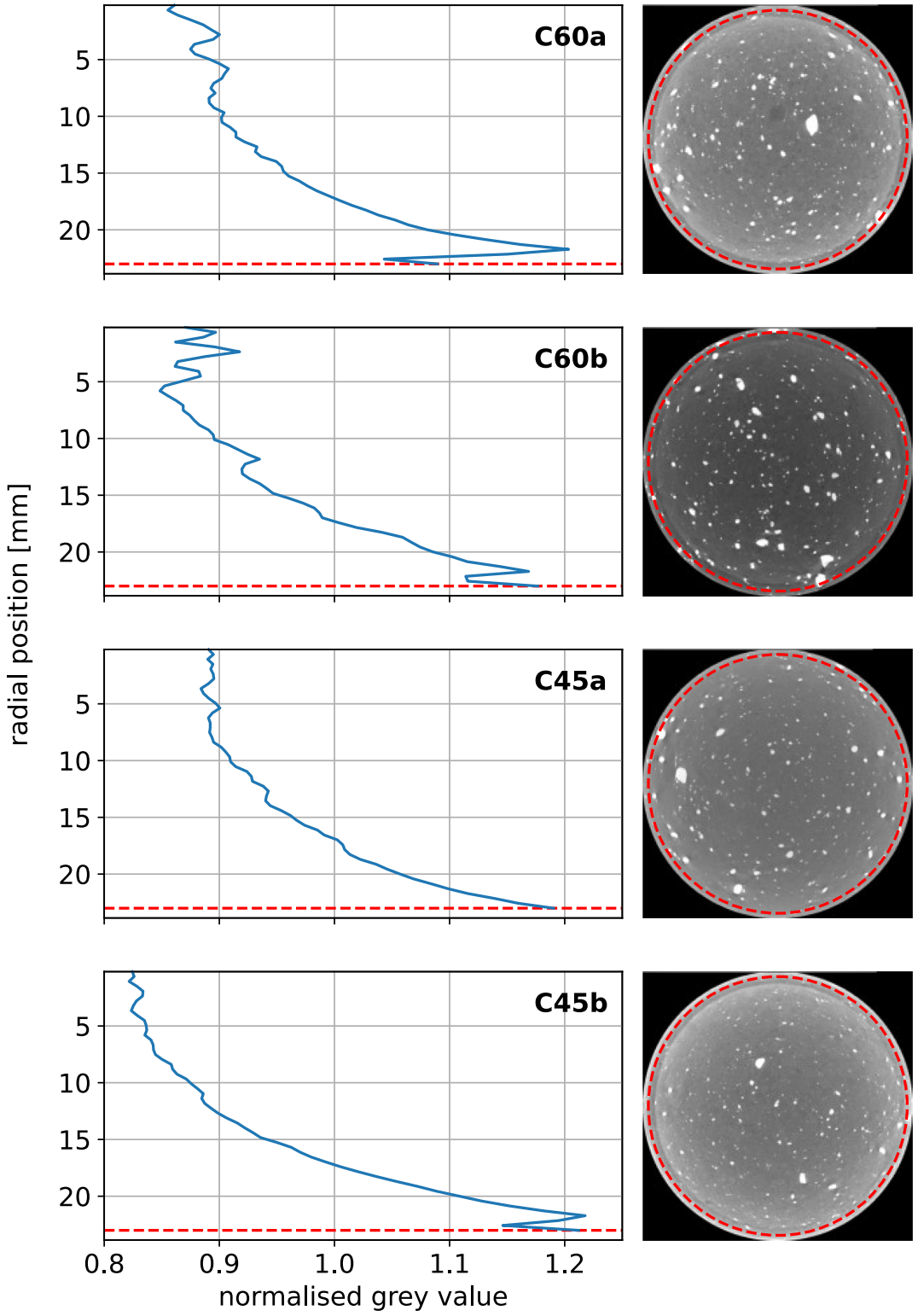

Fig. D.4. Normalised grey Values as a function of the radial distance from the sample central axis within the analysed region of the compressed samples.

Appendix E. Size and spatial distribution of pores and dense clumps

See Figs. E.1–E.4.

Data availability

The raw/processed data required to reproduce these findings will be shared on reasonable request to the corresponding author.

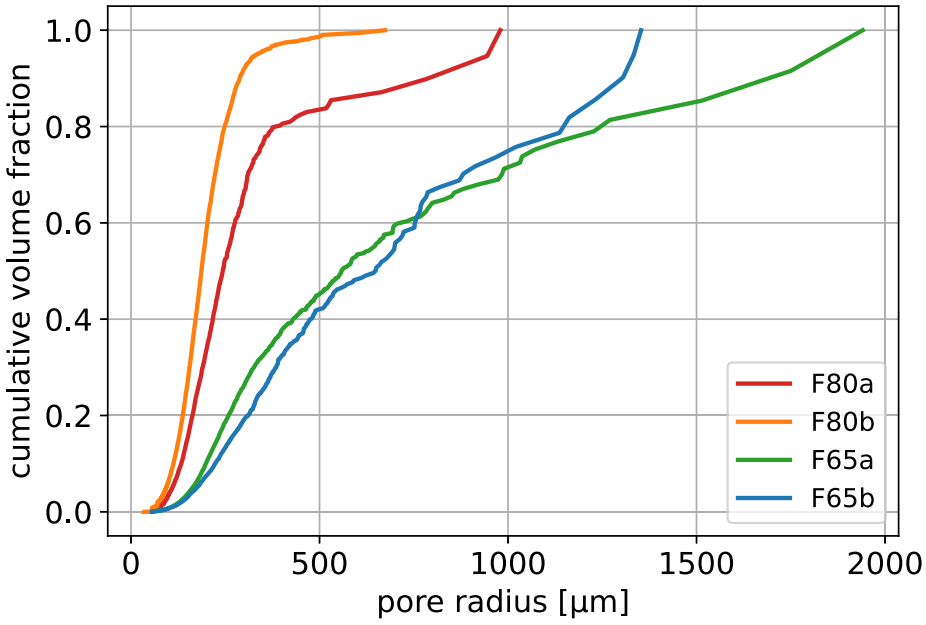

Fig. E.1. Cumulative volume distribution of pores in the freeze-dried samples as a function of the effective pore radius.

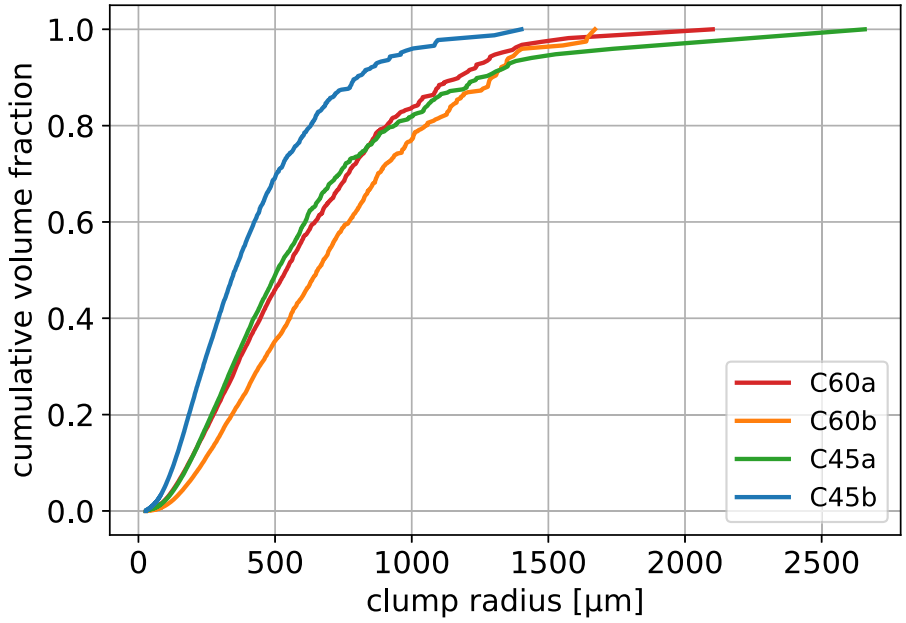

Fig. E.2. Cumulative volume distribution of dense clumps in the compressed samples as a function of the effective clump radius.

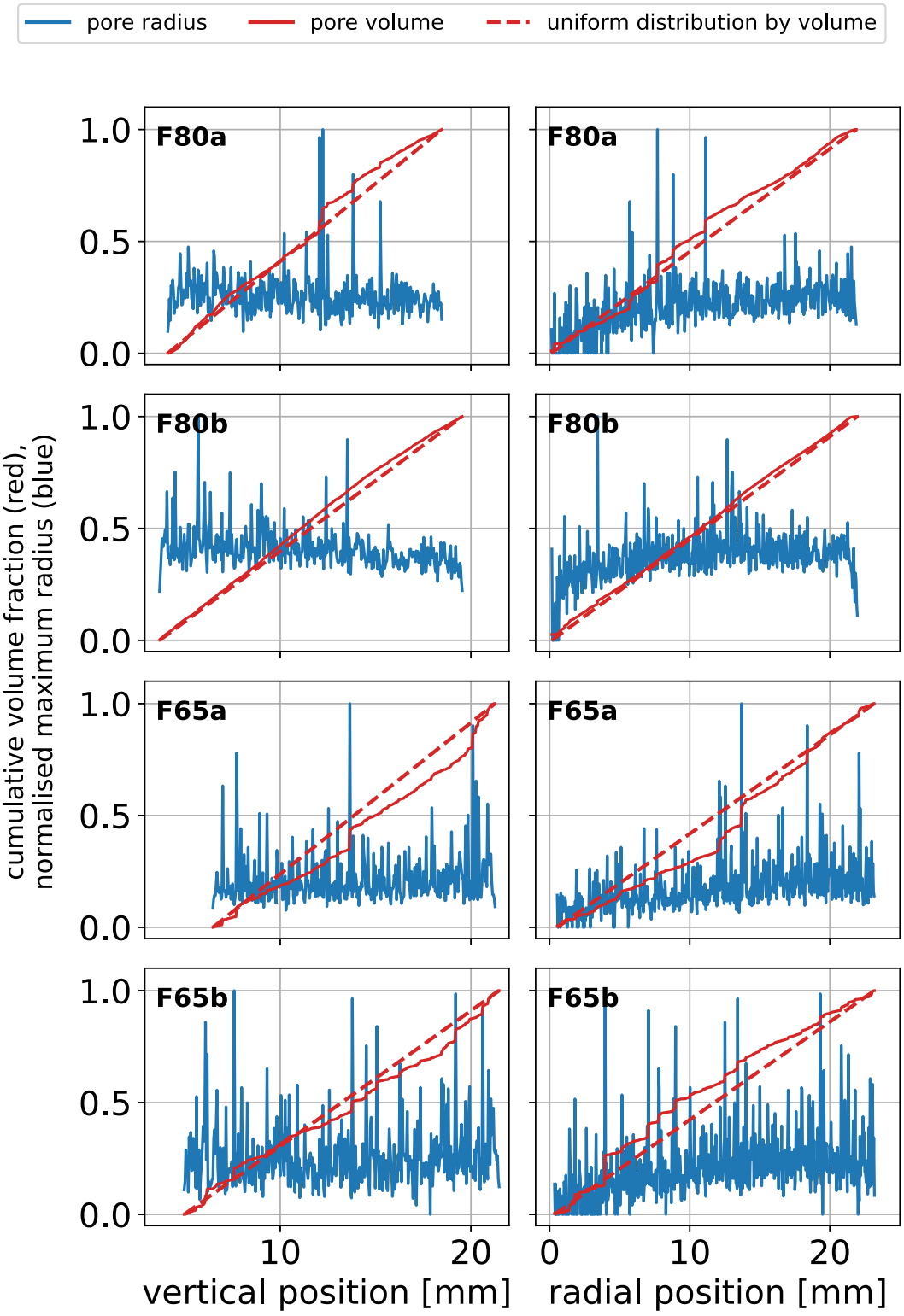

Fig. E.3. Distribution of the maximum effective pore radius, normalised to the global maximum effective pore radius, and cumulative pore volume distribution as a function of vertical position and radial distance from the sample central axis in the freeze-dried samples, normalised to the analysed volume interval.

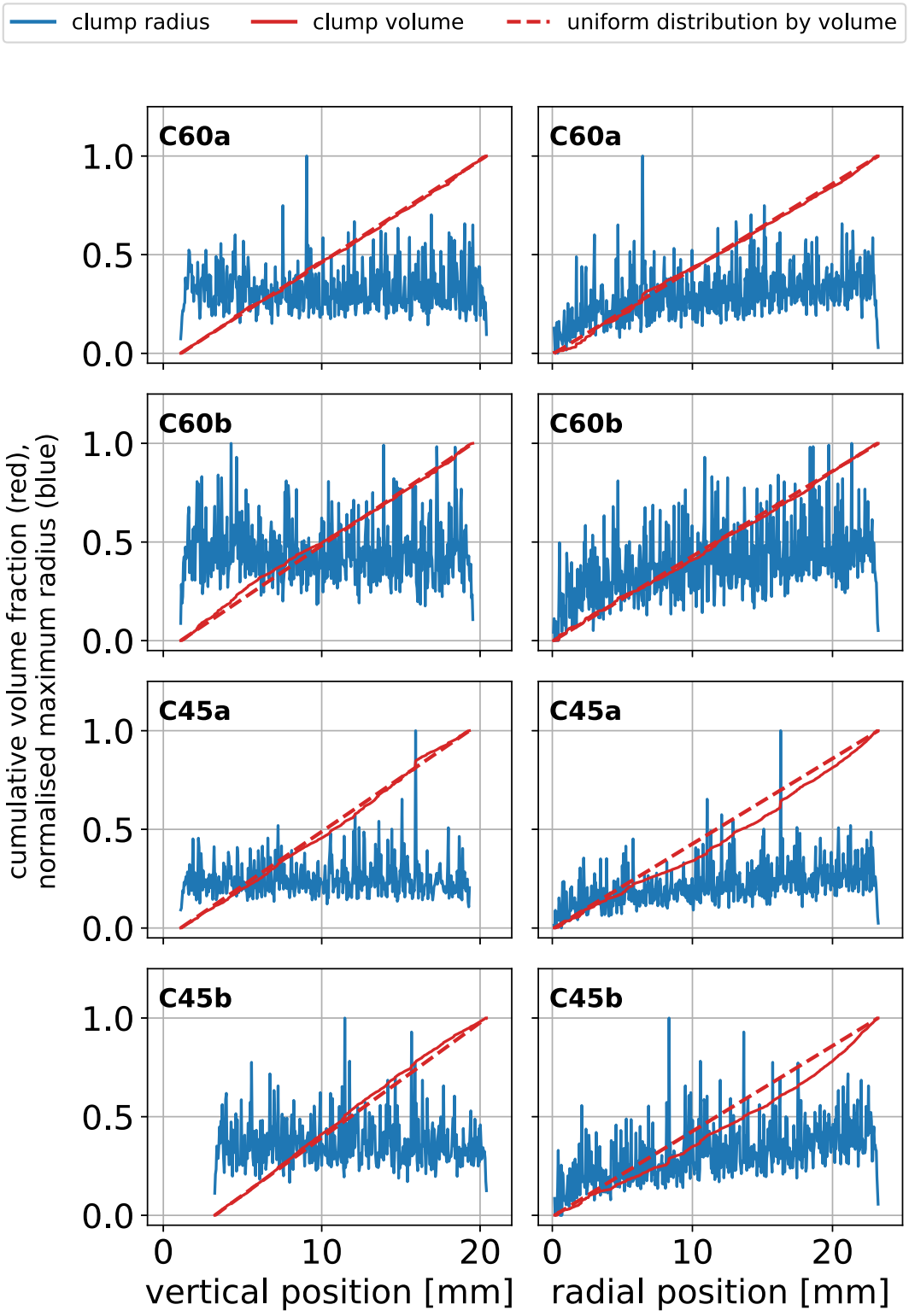

Fig. E.4. Distribution of the maximum effective clump radius, normalised to the global maximum effective clump radius, and cumulative clump volume distribution as a function of vertical position and radial distance from the sample central axis in the compressed samples, normalised to the analysed volume interval.

References

Avdellidou, C., Di Donna, A., Schultz, C., Harthong, B., Price, M.C., Peyroux, R., Britt, D., Cole, M., Delbo', M., 2020. Very weak carbonaceous asteroid simulants I: Mechanical properties and response to hypervelocity impacts. Icarus 341.

Bazi, B., Tack, P., Lindner, M., Vekemans, B., De Pauw, E., Tkalcec, B., Brenker, F.E., Garrevoet, J., Falkenberg, G., Yabuta, H., Yurimoto, H., Nakamura, T., Amano, K., Matsumoto, M., Fujioka, Y., Enokido, Y., Nakashima, D., Uesugi, M., Naraoka, H., Noguchi, T., Okazaki, R., Sakamoto, K., Yada, T., Nishimura, M., Nakato, A., Miyazaki, A., Yogata, K., Abe, M., Okada, T., Usui, T., Yoshikawa, M., Saiki, T., Tanaka, S., Terui, F., Nakazawa, S., Tachibana, S., Watanabe, S.i., Tsuda, Y., Vincze, L., 2022. Trace-element analysis of mineral grains in Ryugu rock fragment sections by synchrotron-based confocal X-ray fluorescence. Earth, Planets Space 74.

Belzile, N., Chen, Y.W., Cai, M.F., Li, Y., 2004. A review on pyrrhotite oxidation. J. Geochem. Explor. 84, 65–76.

Biele, J., Kührt, E., Senshu, H., Sakatani, N., Ogawa, K., Hamm, M., Grott, M., Okada, T., Arai, T., 2019. Effects of dust layers on thermal emission from airless bodies. Prog. Earth Planet. Sci. 6.

Blum, J., Schräpler, R., 2004. Structure and mechanical properties of high-porosity macroscopic agglomerates formed by random ballistic deposition. Phys. Rev. Lett. 93.

Borella, L., Rozo, A., Perfetti, C., Iorio, C.S., 2023. Characterization of composite freeze-dried aerogels with simulant lunar regolith for space applications. Materials 16.

Britt, D.T., Cannon, K.M., Donaldson Hanna, K., Hogancamp, J., Poch, O., Beck, P., Martin, D., Escrig, J., Bonal, L., Metzger, P.T., 2019. Simulated asteroid materials based on carbonaceous chondrite mineralogies. Meteorit. Planet. Sci. 54, 2067–2082.

Brooks, R.A., Chiro, G.D., 1976. Beam hardening in X-ray reconstructive tomography. Phys. Med. Biol. 21, 390–398.

Cambioni, S., Delbo, M., Poggiali, G., Avdellidou, C., Ryan, A.J., Deshapriya, J.D.P., Asphaug, E., Ballouz, R.L., Barucci, M.A., Bennett, C.A., Bottke, W.F., Brucato, J.R., Burke, K.N., Cloutis, E., DellaGiustina, D.N., Emery, J.P., Rozitis, B., Walsh, K.J., Lauretta, D.S., 2021. Fine-regolith production on asteroids controlled by rock porosity. Nature 598, 49–52.

Carnahan, E., Wolfenbarger, N.S., Jordan, J.S., Hesse, M.A., 2021. New insights into temperature-dependent ice properties and their effect on ice shell convection for icy ocean worlds. Earth Planet. Sci. Lett. 563.

Carrasco, S., Cantor, D., Ovalle, C., Dubois, F., 2025. Particle shape distribution effects on the critical strength of granular materials. Comput. Geotech. 177.

Cermak, V., Rybach, L., 1982. 4. Thermal properties: Thermal conductivity and specific heat of minerals and rocks.. In: Angenheister, G. (Ed.), Zahlenwerte and Funktionen Aus Naturwissenschaften Und Technik, Neue Serie, Physikalische Eigenschaften Der Gesteine. Springer-Verlag, pp. 305–343.

Colombani, J., Bert, J., 2007. Holographic interferometry study of the dissolution and diffusion of gypsum in water. Geochim. Cosmochim. Acta 71, 1913–1920.

Deville, S., 2013. Ice-templating, freeze casting: Beyond materials processing. J. Mater. Res. 28.

Di Stefano, C., Ferro, V., Mirabile, S., 2010. Comparison between grain-size analyses using laser diffraction and sedimentation methods. Biosyst. Eng. 106, 205–215.

Diment, W.H., Pratt, H.R., 1988. Thermal Conductivity of Some Rock-Forming Minerals: A Tabulation. Technical Report.

Fujii, N., Ito, K., Miyamoto, M., 1981. Vibrational fracturing rate: A new strength measure for chondrites. In: Lunar and Planetary Science Conference. pp. 312–314.

Fujiya, W., Kawasaki, N., Nagashima, K., Sakamoto, N., O'D. Alexander, C.M., Kita, N.T., Kitajima, K., Abe, Y., Aléon, J., Amari, S., Amelin, Y., Bajo, K.i., Bizzarro, M., Bouvier, A., Carlson, R.W., Chaussidon, M., Choi, B.G., Dauphas, N., Davis, A.M., Di Rocco, T., Fukai, R., Gautam, I., Haba, M.K., Hibiya, Y., Hidaka, H., Homma, H., Hoppe, P., Huss, G.R., Ichida, K., Iizuka, T., Ireland, T.R., Ishikawa, A., Itoh, S., Kleine, T., Komatani, S., Krot, A.N., Liu, M.C., Masuda, Y., McKeegan, K.D., Morita, M., Motomura, K., Moynier, F., Nakai, I., Nguyen, A., Nittler, L., Onose, M., Pack, A., Park, C., Piani, L., Qin, L., Russell, S.S., Schönbächler, M., Tafla, L., Tang, H., Terada, K., Terada, Y., Usui, T., Wada, S., Wadhwa, M., Walker, R.J., Yamashita, K., Yin, Q.Z., Yokoyama, T., Yoneda, S., Young, E.D., Yui, H., Zhang, A.C., Nakamura, T., Naraoka, H., Noguchi, T., Okazaki, R., Sakamoto, K., Yabuta, H., Abe, M., Miyazaki, A., Nakato, A., Nishimura, M., Okada, T., Yada, T., Yogata, K., Nakazawa, S., Saiki, T., Tanaka, S., Terui, F., Tsuda, Y., Watanabe, S.i., Yoshikawa, M., Tachibana, S., Yurimoto, H., 2023. Carbonate record of temporal change in oxygen fugacity and gaseous species in asteroid Ryugu. Nat. Geosci. 16, 675–682.

Garcia, X., Akanji, L.T., Blunt, M.J., Matthai, S.K., Latham, J.P., 2009. Numerical study of the effects of particle shape and polydispersity on permeability. Phys. Rev. E 80.

Gattacceca, J., Gounelle, M., Devouard, B., Barrat, J.A., Bonal, L., King, A.J., Maurel, C., Beck, P., Roskosz, M., Viennet, J.C., Mukherjee, D., Dauphas, N., Heck, P.R., Yokoyama, T., López García, K., Poch, O., Grauby, O., Harrison, C.S., Vinogradoff, V., Vernazza, P., Tikoo, S., Vidal, V., Rochette, P., AuYang, D., Borschneck, D., Juraszek, J., Clark, B., 2025. Oued Chebeika 002: A new CI1 meteorite linked to outer solar system bodies. Meteorit. Planet. Sci. 60, 1441–1479.

German, R.M., 1996. Sintering Theory and Practice. Wiley.

Grott, M., Knollenberg, J., Hamm, M., Ogawa, K., Jaumann, R., Otto, K.A., Delbo, M., Michel, P., Biele, J., Neumann, W., Knapmeyer, M., Kührt, E., Senshu, H., Okada, T., Helbert, J., Maturilli, A., Müller, N., Hagermann, A., Sakatani, N., Tanaka, S., Arai, T., Mottola, S., Tachibana, S., Pelivan, I., Drube, L., Vincent, J.B., Yano, H., Pilorget, C., Matz, K.D., Schmitz, N., Koncz, A., Schröder, S.E., Trauthan, F., Schlotterer, M., Krause, C., Ho, T.M., Moussi-Soffys, A., 2019. Low thermal conductivity boulder with high porosity identified on C-type asteroid (162173) Ryugu. Nat. Astron. 3, 971–976.

Gundlach, B., Blum, J., 2013. A new method to determine the grain size of planetary regolith. Icarus 223, 479–492.

Guntoro, P., Ghorbani, Y., Koch, P.H., Rosenkranz, J., 2019. X-ray microcomputed tomography (μ CT) for mineral characterization: A review of data analysis methods. Minerals 9.

Haack, D., Otto, K., Gundlach, B., Kreuzig, C., Bischoff, D., Kührt, E., Blum, J., 2020. Tensile strength of dust-ice mixtures and their relevance as cometary analog material. Astron. Astrophys. 642.

Hamm, M., Strauß, M., Grott, M., Knollenberg, J., Luther, R., Biele, J., Senshu, H., 2025. Low thermal inertia of (162173) Ryugu a result of horizontal cracks in boulders. Icarus 430.

Hazen, R.M., Morrison, S.M., Prabhu, A., 2021. An evolutionary system of mineralogy. Part III: Primary chondrule mineralogy (4566 to 4561 Ma). Am. Mineral. 106, 325–350.

Henke, S., Gail, H.P., Trieloff, M., 2016. Thermal evolution and sintering of chondritic planetesimals: III. Modelling the heat conductivity of porous chondrite material. Astron. Astrophys. 589.

Hildebrand, A., Hanton, L., Rankin, M., Ibrahim, M., 2015. An asteroid regolith simulant for hydrated carbonaceous chondrite lithologies (HCCL-1). #5368.

Hildebrand, A.R., McCausland, P.J.A., Brown, P.G., Longstaffe, F.J., Russell, S.D.J., Tagliaferri, E., Wacker, J.F., Mazur, M.J., 2006. The fall and recovery of the Tagish Lake meteorite. Meteorit. Planet. Sci. 41, 407–431.

Hossain, S.S., Bullard, J.W., 2025. Fabrication of intricate lunar regolith monoliths via freeze casting. J. Eur. Ceram. Soc. 45.

Ignashova, L., Brener, A., Altukhov, A., Zhukova, T., Tenizbayev, Y., 2023. Modelling the Clusters Aggregation and Aggregative Stability of Suspensions. Chem. Eng. Trans. 101, 175–180.

Ito, M., Tomioka, N., Uesugi, M., Yamaguchi, A., Shirai, N., Ohigashi, T., Liu, M.C., Greenwood, R.C., Kimura, M., Imae, N., Uesugi, K., Nakato, A., Yogata, K., Yuzawa, H., Kodama, Y., Tsuchiyama, A., Yasutake, M., Findlay, R., Franchi, I.A., Malley, J.A., McCain, K.A., Matsuda, N., McKeegan, K.D., Hirahara, K., Takeuchi, A., Sekimoto, S., Sakurai, I., Okada, I., Karouji, Y., Arakawa, M., Fujii, A., Fujimoto, M., Hayakawa, M., Hirata, N., Hirata, N., Honda, R., Honda, C., Hosoda, S., Iijima, Y.i., Ikeda, H., Ishiguro, M., Ishihara, Y., Iwata, T., Kawahara, K., Kikuchi, S., Kitazato, K., Matsumoto, K., Matsuoka, M., Michikami, T., Mimasu, Y., Miura, A., Mori, O., Morota, T., Nakazawa, S., Namiki, N., Noda, H., Noguchi, R., Ogawa, N., Ogawa, K., Okada, T., Okamoto, C., Ono, G., Ozaki, M., Saiki, T., Sakatani, N., Sawada, H., Senshu, H., Shimaki, Y., Shirai, K., Sugita, S., Takei, Y., Takeuchi, H., Tanaka, S., Tatsumi, E., Terui, F., Tsukizaki, R., Wada, K., Yamada, M., Yamada, T., Yamamoto, Y., Yano, H., Yokota, Y., Yoshihara, K., Yoshikawa, M., Yoshikawa, K., Fukai, R., Furuya, S., Hatakeda, K., Hayashi, T., Hitomi, Y., Kumagai, K., Miyazaki, A., Nishimura, M., Soejima, H., Iwamae, A., Yamamoto, D., Yoshitake, M., Yada, T., Abe, M., Usui, T., Watanabe, S.i., Tsuda, Y., 2022. A pristine record of outer Solar System materials from asteroid Ryugu's returned sample. Nat. Astron. 6, 1163–1171.

Johnson, K.L., Kendall, K., Roberts, A.D., 1971. Surface energy and the contact of elastic solids. Proc. R. Soc. Lond. Ser. A 324, 301–313.

King, A., Phillips, K., Strekopytov, S., Vita-Finzi, C., Russell, S., 2020. Terrestrial modification of the Ivuna meteorite and a reassessment of the chemical composition of the CI type specimen. Geochim. Cosmochim. Acta 268, 73–89.

King, A., Schofield, P., Howard, K., Russell, S., 2015. Modal mineralogy of CI and CI-like chondrites by X-ray diffraction. Geochim. Cosmochim. Acta 165, 148–160.

Klar, L., Glißmann, T., Lammers, K., Güttler, C., Blum, J., 2024. Structural properties of different sphere packings with arbitrary porosities for planetary-science applications. Granul. Matter 26, 59.

Kohout, T., Čuda, J., Filip, J., Britt, D., Bradley, T., Tuček, J., Skála, R., Kletetschka, G., Kašlík, J., Malina, O., Šišková, K., Zbořil, R., 2014. Space weathering simulations through controlled growth of iron nanoparticles on olivine. Icarus 237, 75–83.

Kosowska-Golachowska, M., Gajewski, W., Musiał, T., 2014. Determination of the effective thermal conductivity of solid fuels by the laser flash method. Arch. Thermodyn. 35, 3–16.

Lauretta, D.S., Connolly, H.C., Aebersold, J.E., Alexander, C.M.O., Ballouz, R.L., Barnes, J.J., Bates, H.C., Bennett, C.A., Blanche, L., Blumenfeld, E.H., Clemett, S.J., Cody, G.D., DellaGiustina, D.N., Dworkin, J.P., Eckley, S.A., Foustoukos, D.I., Franchi, I.A., Glavin, D.P., Greenwood, R.C., Haenecour, P., Hamilton, V.E., Hill, D.H., Hiroi, T., Ishimaru, K., Jourdan, F., Kaplan, H.H., Keller, L.P., King, A.J., Koefoed, P., Kontogiannis, M.K., Le, L., Macke, R.J., McCoy, T.J., Milliken, R.E., Najorka, J., Nguyen, A.N., Pajola, M., Polit, A.T., Righter, K., Roper, H.L., Russell, S.S., Ryan, A.J., Sandford, S.A., Schofield, P.F., Schultz, C.D., Seifert, L.B., Tachibana, S., Thomas-Keprta, K.L., Thompson, M.S., Tu, V., Tusberti, F., Wang, K., Zega, T.J., Wolner, C.W.V., the OSIRIS-REx Sample Analysis Team, 2024. Asteroid (101955) Bennu in the laboratory: Properties of the sample collected by OSIRIS-REx. Meteorit. Planet. Sci. 59, 2453–2486.

Lauretta, D.S., Enos, H.L., Polit, A.T., Roper, H.L., Wolner, C.W., 2021. OSIRIS-REx at Bennu: Overcoming challenges to collect a sample of the early Solar System. In: Sample Return Missions. Elsevier, pp. 163–194.

Leroux, H., Le Guillou, C., Bernard, S., Marinova, M., Laforet, S., 2023. Organics in Ryugu, Orgueil and other chondrites analyzed in situ by STXM and TEM. In: Annual Goldschmidt Conference.

Libourel, G., Nakamura, A.M., Beck, P., Potin, S., Ganino, C., Jacomet, S., Ogawa, R., Hasegawa, S., Michel, P., 2020. Hypervelocity impacts on iron meteorite targets: Understanding impact processes on metal-rich asteroids. In: 51st Annual Lunar and Planetary Science Conference.

Lodders, K., Palme, H., Gail, H.P., 2009. Abundances of the elements in the solar system. Landolt Börnstein 4B.

López-Oquendo, A.J., Loeffler, M.J., Trilling, D.E., 2024. Laser irradiation of carbonaceous chondrite simulants: Space-weathering implications for C-complex asteroids. Planet. Sci. J. 5.

Marrocchi, Y., Avice, G., Barrat, J.A., 2021. The Tarda Meteorite: A window into the formation of D-type asteroids. Astrophys. J. Lett. 913.

McCain, K.A., Matsuda, N., Liu, M.C., McKeegan, K.D., Yamaguchi, A., Kimura, M., Tomioka, N., Ito, M., Imae, N., Uesugi, M., Shirai, N., Ohigashi, T., Greenwood, R.C., Uesugi, K., Nakato, A., Yogata, K., Yuzawa, H., Kodama, Y., Hirahara, K., Sakurai, I., Okada, I., Karouji, Y., Nakazawa, S., Okada, T., Saiki, T., Tanaka, S., Terui, F., Yoshikawa, M., Miyazaki, A., Nishimura, M., Yada, T., Abe, M., Usui, T., Watanabe, S.i., Tsuda, Y., 2023. Early fluid activity on Ryugu inferred by isotopic analyses of carbonates and magnetite. Nat. Astron. 7, 309–317.

Metzger, P.T., Britt, D.T., Covey, S., Schultz, C., Cannon, K.M., Grossman, K.D., Mantovani, J.G., Mueller, R.P., 2019. Measuring the fidelity of asteroid regolith and cobble simulants. Icarus 321, 632–646.

Michikami, T., Honda, C., Miyamoto, H., Hirabayashi, M., Hagermann, A., Irie, T., Nomura, K., Ernst, C.M., Kawamura, M., Sugimoto, K., Tatsumi, E., Morota, T., Hirata, N., Noguchi, T., Cho, Y., Kameda, S., Kouyama, T., Yokota, Y., Noguchi, R., Hayakawa, M., Hirata, N., Honda, R., Matsuoka, M., Sakatani, N., Suzuki, H., Yamada, M., Yoshioka, K., Sawada, H., Hemmi, R., Kikuchi, H., Ogawa, K., Watanabe, S.i., Tanaka, S., Yoshikawa, M., Tsuda, Y., Sugita, S., 2019. Boulder size and shape distributions on asteroid Ryugu. Icarus 331, 179–191.

Miyamoto, H., Niihara, T., 2021. Simplified simulated materials of asteroid Ryugu for spacecraft operations and scientific evaluations. Nat. Resour. Res. 30, 3035–3044.

Miyamoto, H., Niihara, T., Wada, K., Ogawa, K., Senshu, H., Michel, P., Kikuchi, H., Hemmi, R., Nakamura, T., Nakamura, A.M., Hirata, N., Sasaki, S., Asphaug, E., Britt, D.T., Abell, P.A., Ballouz, R.L., Banouin, O.S., Baresi, N., Barucci, M.A., Biele, J., Grott, M., Hino, H., Hong, P.K., Imada, T., Kameda, S., Kobayashi, M., Libourel, G., Mogi, K., Murdoch, N., Nishio, Y., Okamoto, S., Ota, Y., Otsuki, M., Otto, K.A., Sakatani, N., Shimizu, Y., Takemura, T., Terada, N., Tsukamoto, M., Usui, T., Willner, K., 2021. Surface environment of Phobos and Phobos simulant UTPS. Earth, Planets Space 73.

Molaro, J.L., Byrne, S., Le, J.L., 2017. Thermally induced stresses in boulders on airless body surfaces, and implications for rock breakdown. Icarus 294, 247–261.

Nakamura, E., Kobayashi, K., Tanaka, R., Kunihiro, T., Kitagawa, H., Potiszil, C., Ota, T., Sakaguchi, C., Yamanaka, M., Ratnayake, D.M., Tripathi, H., Kumar, R., Avramescu, M.L., Tsuchida, H., Yachi, Y., Miura, H., Abe, M., Fukai, R., Furuya, S., Hatakeda, K., Hayashi, T., Hitomi, Y., Kumagai, K., Miyazaki, A., Nakato, A., Nishimura, M., Okada, T., Soejima, H., Sugita, S., Suzuki, A., Usui, T., Yada, T., Yamamoto, D., Yogata, K., Yoshitake, M., Arakawa, M., Fujii, A., Hayakawa, M., Hirata, N., Hirata, N., Honda, R., Honda, C., Hosoda, S., Iijima, Y.i., Ikeda, H., Ishiguro, M., Ishihara, Y., Iwata, T., Kawahara, K., Kikuchi, S., Kitazato, K., Matsumoto, K., Matsuoka, M., Michikami, T., Mimasu, Y., Miura, A., Morota, T., Nakazawa, S., Namiki, N., Noda, H., Noguchi, R., Ogawa, N., Ogawa, K., Okamoto, C., Ono, G., Ozaki, M., Saiki, T., Sakatani, N., Sawada, H., Senshu, H., Shimaki, Y., Shirai, K., Takei, Y., Takeuchi, H., Tanaka, S., Tatsumi, E., Terui, F., Tsukizaki, R., Wada, K., Yamada, M., Yamada, T., Yamamoto, Y., Yano, H., Yokota, Y., Yoshihara, K., Yoshikawa, M., Yoshikawa, K., Fujimoto, M., Watanabe, S.i., Tsuda, Y., 2022. On the origin and evolution of the asteroid Ryugu: A comprehensive geochemical perspective. Proc. Jpn. Acad. Ser. B 98, 227–282.

Neumann, W., Grott, M., Trieloff, M., Jaumann, R., Biele, J., Hamm, M., Kührt, E., 2021. Microporosity and parent body of the rubble-pile NEA (162173) Ryugu. Icarus 358.

Nishikawara, M., Nagano, H., Mottet, L., Prat, M., 2014. Numerical study of thermal performance of a capillary evaporator in a loop heat pipe with liquid-saturated wick. J. Electron. Cool. Therm. Control. 04, 118–127.

Noguchi, T., Matsumoto, T., Miyake, A., Igami, Y., Haruta, M., Saito, H., Hata, S., Seto, Y., Miyahara, M., Tomioka, N., Ishii, H.A., Bradley, J.P., Ohtaki, K.K., Dobrică, E., Leroux, H., Guillou, C.L., Jacob, D., De La Peña, F., Laforet, S., Mouloud, B.E., Marinova, M., Langenhorst, F., Harries, D., Beck, P., Phan, T.H.V., Rebois, R., Abreu, N.M., Gray, J., Zega, T., Zanetta, P.M., Thompson, M.S., Stroud, R., Burgess, K., Cymes, B.A., Bridges, J.C., Hicks, L., Lee, M.R., Daly, L., Bland, P.A., Smith, W.A., McFadzean, S., Martin, P.E., Bagot, P.A.J., Fougerouse, D., Saxey, D.W., Reddy, S., Rickard, W.D.A., Zolensky, M.E., Frank, D.R., Martinez, J., Tsuchiyama, A., Yasutake, M., Matsuno, J., Okumura, S., Mitsukawa, I., Uesugi, K., Uesugi, M., Takeuchi, A., Sun, M., Enju, S., Takigawa, A., Michikami, T., Nakamura, T., Matsumoto, M., Nakauchi, Y., Abe, M., Nakazawa, S., Okada, T., Saiki, T., Tanaka, S., Terui, F., Yoshikawa, M., Miyazaki, A., Nakato, A., Nishimura, M., Usui, T., Yada, T., Yurimoto, H., Nagashima, K., Kawasaki, N., Sakamotoa, N., Hoppe, P., Okazaki, R., Yabuta, H., Naraoka, H., Sakamoto, K., Tachibana, S., Watanabe, S.i., Tsuda, Y., 2024. Mineralogy and petrology of fine-grained samples recovered from the asteroid (162173) Ryugu. Meteorit. Planet. Sci. 59, 1877–1906.

Okada, T., Fukuhara, T., Tanaka, S., Taguchi, M., Arai, T., Sakatani, N., Shimaki, Y., Senshu, H., Ogawa, Y., Demura, H., Suko, K., Kitazato, K., Kouyama, T., Sekiguchi, T., Takita, J., Hasegawa, S., Matsunaga, T., Wada, T., Imamura, T., Helbert, J., Mueller, T.G., Hagermann, A., Biele, J., Grott, M., Hamm, M., Delbo, M., Yamamoto, Y., Hirata, N., Hirata, N.Y., Terui, F., Saiki, T., Nakazawa, S., Yoshikawa, M., Watanabe, S., Tsuda, T., 2020. Unveiling highly-porous nature of primitve asteroid 162173 Ryugu by thermal imager on Hayabusa2. In: 51st Annual Lunar and Planetary Science Conference.

Omura, T., Nakamura, A.M., 2021. Primordial porous structure of chondrite parent bodies due to self-gravity. Planet. Sci. J. 2.

Oquendo-Patiño, W.F., Estrada, N., 2022. Finding the grain size distribution that produces the densest arrangement in frictional sphere packings: Revisiting and rediscovering the century-old Fuller and Thompson distribution. Phys. Rev. E 105.

Patzek, M., Rüsch, O., Molaro, J.L., 2024. On the response of chondrites to diurnal temperature change—Experimental simulation of asteroidal surface conditions. J. Geophys. Res. (Planets) 129.

Pilorget, C., Okada, T., Bibring, J.P., Loizeau, D., Hatakeda, K., Nardelli, L., Riu, L., Sheppard, R., Jiang, T., Mahlke, M., Brunetto, R., Baklouti, D., Fukai, R., Abe, M., Aléon-Toppani, A., Enokido, Y., Hamm, V., Kawasaki, S., Lantz, C., Miyazaki, A., Moussi-Soffys, A., Nishimura, M., Poulet, F., Tahara, R., Usui, T., Yada, T., Yogata, K., 2025. Bennu and Ryugu constituents from samples IR analyses and potential source of terrestrial planets' ingredients. Nat. Commun. 16.

Plyasunov, A.V., Zyubina, T.S., 2021. Thermodynamic modeling of the solubility of quartz in water up to high temperatures and pressures. ACS Earth Space Chem. 5, 941–959.

Ricardo, D., Hodgkinson, J., Akbar Rhamdhani, M., Brooks, G., 2023. A review on the preparation techniques and geotechnical behaviour of icy lunar regolith simulants. Adv. Space Res. 72, 4553–4581.

Rogers, L., Hill, K., Hawkes, R., 2005. Mass loss due to sputtering and thermal processes in meteoroid ablation. Planet. Space Sci. 53, 1341–1354.

Roquier, G., 2024. A century of granular packing models. Powder Technol. 441.

Rozitis, B., Ryan, A.J., Emery, J.P., Christensen, P.R., Hamilton, V.E., Simon, A.A., Reuter, D.C., Al Asad, M., Ballouz, R.L., Bandfield, J.L., Barnouin, O.S., Bennett, C.A., Bernacki, M., Burke, K.N., Cambioni, S., Clark, B.E., Daly, M.G., Delbo, M., DellaGiustina, D.N., Elder, C.M., Hanna, R.D., Haberle, C.W., Howell, E.S., Golish, D.R., Jawin, E.R., Kaplan, H.H., Lim, L.F., Molaro, J.L., Munoz, D.P., Nolan, M.C., Rizk, B., Siegler, M.A., Susorney, H.C.M., Walsh, K.J., Lauretta, D.S., 2020. Asteroid (101955) Bennu's weak boulders and thermally anomalous equator. Sci. Adv. 6.

Sakatani, N., Ogawa, K., Iijima, Y., Arakawa, M., Honda, R., Tanaka, S., 2017. Thermal conductivity model for powdered materials under vacuum based on experimental studies. AIP Adv. 7.

Sakatani, N., Tanaka, S., Okada, T., Fukuhara, T., Riu, L., Sugita, S., Honda, R., Morota, T., Kameda, S., Yokota, Y., Tatsumi, E., Yumoto, K., Hirata, N., Miura, A., Kouyama, T., Senshu, H., Shimaki, Y., Arai, T., Takita, J., Demura, H., Sekiguchi, T., Müller, T.G., Hagermann, A., Biele, J., Grott, M., Hamm, M., Delbo, M., Neumann, W., Taguchi, M., Ogawa, Y., Matsunaga, T., Wada, T., Hasegawa, S., Helbert, J., Hirata, N., Noguchi, R., Yamada, M., Suzuki, H., Honda, C., Ogawa, K., Hayakawa, M., Yoshioka, K., Matsuoka, M., Cho, Y., Sawada, H., Kitazato, K., Iwata, T., Abe, M., Ohtake, M., Matsuura, S., Matsumoto, K., Noda, H., Ishihara, Y., Yamamoto, K., Higuchi, A., Namiki, N., Ono, G., Saiki, T., Imamura, H., Takagi, Y., Yano, H., Shirai, K., Okamoto, C., Nakazawa, S., Iijima, Y., Arakawa, M., Wada, K., Kadono, T., Ishibashi, K., Terui, F., Kikuchi, S., Yamaguchi, T., Ogawa, N., Mimasu, Y., Yoshikawa, K., Takahashi, T., Takei, Y., Fujii, A., Takeuchi, H., Yamamoto, Y., Hirose, C., Hosoda, S., Mori, O., Shimada, T., Soldini, S., Tsukizaki, R., Ozaki, M., Tachibana, S., Ikeda, H., Ishiguro, M., Yabuta, H., Yoshikawa, M., Watanabe, S., Tsuda, Y., 2021. Anomalously porous boulders on (162173) Ryugu as primordial materials from its parent body. Nat. Astron. 5, 766–774.

Scholz, F., Kahlert, H., 2015. The calculation of the solubility of metal hydroxides, oxide-hydroxides, and oxides, and their visualisation in logarithmic diagrams. ChemTexts 1.

Schön, S., 2011. Thermal properties. In: Handbook of Petroleum Exploration and Production, vol. 8, Elsevier, pp. 337–372.

Schöpfer, M.P., Abe, S., Childs, C., Walsh, J.J., 2009. The impact of porosity and crack density on the elasticity, strength and friction of cohesive granular materials: Insights from DEM modelling. Int. J. Rock Mech. Min. Sci. 46, 250–261.

Serra, C., Grauby, O., Ferry, D., Duvernay, F., Danger, G., Marin-Carbonne, J., Vinogradoff, V., 2025. Experimental investigations of mineral-organic chondritic analogs under hydrothermal conditions: Implications for carbonaceous asteroids. Geochim. Cosmochim. Acta 398, 29–43.

Shen, Y.L., Rose, G., 2024. Combined effects of pores and cracks on the effective thermal conductivity of materials: A numerical study. J. Mater. Sci.: Mater. Eng. 19.

Tachibana, S., 2021. The Hayabusa2 mission: What will we expect from samples from C-type near-Earth asteroid (162173) Ryugu? In: Sample Return Missions. Elsevier, pp. 147–162.

Tachibana, S., 2023. Mineralogy of returned sample from C-type near-earth asteroid (162173) Ryugu. In: Bindi, L., Cruciani, G. (Eds.), Celebrating the International Year of Mineralogy. Springer Nature Switzerland, pp. 265–286.

Takano, Y., Naraoka, H., Dworkin, J.P., Koga, T., Sasaki, K., Sato, H., Oba, Y., Ogawa, N.O., Yoshimura, T., Hamase, K., Ohkouchi, N., Parker, E.T., Aponte, J.C., Glavin, D.P., Furukawa, Y., Aoki, J., Kano, K., Nomura, S.i.M., Orthous-Daunay, F.R., Schmitt-Kopplin, P., Hayabusa2-initial-analysis SOM team, Furusho, A., Hashiguchi, M., Fukushima, K., Dan Aoki, McLain, H.L., Elsila, J.E., Graham, H.V., Eiler, J.M., Hertkorn, N., Ruf, A., Wolters, C., Isa, J., Vuitton, V., Thissen, R., Sakai, S., Sugahara, H., Mita, H., Chikaraishi, Y., Yoshikawa, T., Tanaka, S., Morita, M., Onose, M., Araoka, D., Kabashima, F., Fujishima, K., Sato, H., Yamazaki, T., Kimura, Y., Yurimoto, H., Nakamura, T., Noguchi, T., Okazaki, R., Yabuta, H., Sakamoto, K., Yada, T., Nishimura, M., Nakato, A., Miyazaki, A., Yogata, K., Abe, M., Okada, T., Usui, T., Yoshikawa, M., Saiki, T., Tanaka, S., Terui, F., Nakazawa, S., Watanabe, S.i., Tsuda, Y., Tachibana, S., 2024. Primordial aqueous alteration recorded in water-soluble organic molecules from the carbonaceous asteroid (162173) Ryugu. Nat. Commun. 15.

Taylor, G.H., Teichmüller, M., Davis, A., Diessel, C.F.K., Littke, R., Robert, P., 1998. Organic Petrology: A New Handbook Incorporating Some Revised Parts of Stach's Textbook of Coal Petrology. Gebrüder Borntraeger.

Tomioka, N., Yamaguchi, A., Ito, M., Uesugi, M., Imae, N., Shirai, N., Ohigashi, T., Kimura, M., Liu, M.C., Greenwood, R.C., Uesugi, K., Nakato, A., Yogata, K., Yuzawa, H., Kodama, Y., Hirahara, K., Sakurai, I., Okada, I., Karouji, Y., Okazaki, K., Kurosawa, K., Noguchi, T., Miyake, A., Miyahara, M., Seto, Y., Matsumoto, T., Igami, Y., Nakazawa, S., Okada, T., Saiki, T., Tanaka, S., Terui, F., Yoshikawa, M., Miyazaki, A., Nishimura, M., Yada, T., Abe, M., Usui, T., Watanabe, S.i., Tsuda, Y., 2023. A history of mild shocks experienced by the regolith particles on hydrated asteroid Ryugu. Nat. Astron. 669–677.

Tsuchiyama, A., Matsumoto, M., Matsuno, J., Yasutake, M., Nakamura, T., Noguchi, T., Miyake, A., Uesugi, K., Takeuchi, A., Okumura, S., Fujioka, Y., Sun, M., Takigawa, A., Matsumoto, T., Enju, S., Mitsukawa, I., Enokido, Y., Kawamoto, T., Mikouchi, T., Michikami, T., Morita, T., Kikuiri, M., Amano, K., Kagawa, E., Rubino, S., Dionnet, Z., Aléon-Toppani, A., Brunetto, R., Zolensky, M.E., Nakano, T., Nakano, N., Yurimoto, H., Okazaki, R., Yabuta, H., Naraoka, H., Sakamoto, K., Yada, T., Nishimura, M., Nakato, A., Miyazaki, A., Yogata, K., Abe, M., Okada, T., Usui, T., Yoshikawa, M., Saiki, T., Tanaka, S., Nakazawa, S., Terui, F., Tachibana, S., Watanabe, S.i., Tsuda, Y., 2024. Three-dimensional textures of Ryugu samples and their implications for the evolution of aqueous alteration in the Ryugu parent body. Geochim. Cosmochim. Acta 375, 146–172.

Wargnier, A., Gautier, T., Doressoundiram, A., Poggiali, G., Beck, P., Poch, O., Quirico, E., Nakamura, T., Miyamoto, H., Kameda, S., Hasselmann, P.H., Ruscassier, N., Buch, A., Fornasier, S., Barucci, M.A., 2024. Spectro-photometry of Phobos simulants. Icarus 421.

Wargnier, A., Poch, O., Poggiali, G., Gautier, T., Doressoundiram, A., Beck, P., Nakamura, T., Miyamoto, H., Kameda, S., Ruscassier, N., Buch, A., Hasselmann, P.H., Sultana, R., Quirico, E., Fornasier, S., Barucci, M.A., 2025. Spectro-photometry of Phobos simulants II. Effects of porosity and texture. Icarus 438.

Weibel, E.R., Elias, H., 1967. Introduction to stereologic principles. In: Weibel, E.R., Elias, H. (Eds.), Quantitative Methods in Morphology / Quantitative Methoden in Der Morphologie. Springer Berlin Heidelberg, pp. 89–98.

Whitney, G., 1983. Hydrothermal reactivity of saponite. Clays Clay Miner. 31, 1–8.

Yamaguchi, A., Tomioka, N., Ito, M., Shirai, N., Kimura, M., Greenwood, R.C., Liu, M.C., McCain, K.A., Matsuda, N., Uesugi, M., Imae, N., Ohigashi, T., Uesugi, K., Nakato, A., Yogata, K., Yuzawa, H., Kodama, Y., Hirahara, K., Sakurai, I., Okada, I., Karouji, Y., Nakazawa, S., Okada, T., Saiki, T., Tanaka, S., Terui, F., Yoshikawa, M., Miyazaki, A., Nishimura, M., Yada, T., Abe, M., Usui, T., Watanabe, S.i., Tsuda, Y., 2023. Insight into multi-step geological evolution of C-type asteroids from Ryugu particles. Nat. Astron. 7, 398–405.

Yokoyama, T., Nagashima, K., Nakai, I., Young, E.D., Abe, Y., Aléon, J., Alexander, C.M.O., Amari, S., Amelin, Y., Bajo, K.i., Bizzarro, M., Bouvier, A., Carlson, R.W., Chaussidon, M., Choi, B.G., Dauphas, N., Davis, A.M., Di Rocco, T., Fujiya, W., Fukai, R., Gautam, I., Haba, M.K., Hibiya, Y., Hidaka, H., Homma, H., Hoppe, P., Huss, G.R., Ichida, K., Iizuka, T., Ireland, T.R., Ishikawa, A., Ito, M., Itoh, S., Kawasaki, N., Kita, N.T., Kitajima, K., Kleine, T., Komatani, S., Krot, A.N., Liu, M.C., Masuda, Y., McKeegan, K.D., Morita, M., Motomura, K., Moynier, F., Nguyen, A., Nittler, L., Onose, M., Pack, A., Park, C., Piani, L., Qin, L., Russell, S.S., Sakamoto, N., Schönbächler, M., Tafla, L., Tang, H., Terada, K., Terada, Y., Usui, T., Wada, S., Wadhwa, M., Walker, R.J., Yamashita, K., Yin, Q.Z., Yoneda, S., Yui, H., Zhang, A.C., Connolly, H.C., Lauretta, D.S., Nakamura, T., Naraoka, H., Noguchi, T., Okazaki, R., Sakamoto, K., Yabuta, H., Abe, M., Arakawa, M., Fujii, A., Hayakawa, M., Hirata, N., Hirata, N., Honda, R., Honda, C., Hosoda, S., Iijima, Y.i., Ikeda, H., Ishiguro, M., Ishihara, Y., Iwata, T., Kawahara, K., Kikuchi, S., Kitazato, K., Matsumoto, K., Matsuoka, M., Michikami, T., Mimasu, Y., Miura, A., Morota, T., Nakazawa, S., Namiki, N., Noda, H., Noguchi, R., Ogawa, N., Ogawa, K., Okada, T., Okamoto, C., Ono, G., Ozaki, M., Saiki, T., Sakatani, N., Sawada, H., Senshu, H., Shimaki, Y., Shirai, K., Sugita, S., Takei, Y., Takeuchi, H., Tanaka, S., Tatsumi, E., Terui, F., Tsuda, Y., Tsukizaki, R., Wada, K., Watanabe, S.i., Yamada, M., Yamada, T., Yamamoto, Y., Yano, H., Yokota, Y., Yoshihara, K., Yoshikawa, M., Yoshikawa, K., Furuya, S., Hatakeda, K., Hayashi, T., Hitomi, Y., Kumagai, K., Miyazaki, A., Nakato, A., Nishimura, M., Soejima, H., Suzuki, A., Yada, T., Yamamoto, D., Yogata, K., Yoshitake, M., Tachibana, S., Yurimoto, H., 2023. Samples returned from the asteroid Ryugu are similar to Ivuna-type carbonaceous meteorites. Science 379.

Yoshikawa, M., Kawaguchi, J., Fujiwara, A., Tsuchiyama, A., 2021. The Hayabusa mission. In: Sample Return Missions. Elsevier, pp. 123–146.

Yuan, G., Cao, Y., Schulz, H.M., Hao, F., Gluyas, J., Liu, K., Yang, T., Wang, Y., Xi, K., Li, F., 2019. A review of feldspar alteration and its geological significance in sedimentary basins: From shallow aquifers to deep hydrocarbon reservoirs. Earth-Sci. Rev. 191, 114–140.

Zhou, Z.Y., Zou, R.P., Pinson, D., Yu, A.B., 2011. Dynamic simulation of the packing of ellipsoidal particles. Ind. Eng. Chem. Res. 50, 9787–9798.

Zivithal, S., Kargl, G., Macher, W., Laddha, S., Blum, J., Gundlach, B., Güttler, C., Sierks, H., 2024. Grain polydispersity and non-sphericity effects on gas flow through granular beds using measurements and modelling. Mon. Not. R. Astron. Soc. 531, 3642–3657.